Monthly Notices
of the
ROYAL ASTRONOMICAL SOCIETY

MNRAS **468,** 1273–1299 (2017)
Advance Access publication 2017 January 23

doi:10.1093/mnras/stx173

# Growing supermassive black holes in the late stages of galaxy mergers are heavily obscured

C. Ricci,[1,2,3★] F. E. Bauer,[1,2,4,5] E. Treister,[1,2] K. Schawinski,[6] G. C. Privon,[1,2] L. Blecha,[7] P. Arevalo,[8] L. Armus,[9] F. Harrison,[10] L. C. Ho,[3,11] K. Iwasawa,[12,13] D. B. Sanders[14] and D. Stern[15]

[1]*Facultad de Física, Instituto de Astrofísica, Pontificia Universidad Católica de Chile, Casilla 306, Santiago 22, 8970117 Chile*
[2]*EMBIGGEN Anillo, Concepcion, 4030000 Chile*
[3]*Kavli Institute for Astronomy and Astrophysics, Peking University, Beijing 100871, China*
[4]*Space Science Institute, 4750 Walnut Street, Suite 205, Boulder, CO 80301, USA*
[5]*Millenium Institute of Astrophysics, Santiago, 7600740 Chile*
[6]*Department of Physics, Institute for Astronomy, ETH Zurich, Wolfgang-Pauli-Strasse 27, CH-8093 Zurich, Switzerland*
[7] *Department of Astronomy, University of Maryland, 1113 PSC, Bldg. 415, College Park, MD 20742, USA*
[8]*Facultad de Ciencias, Instituto de Física y Astronomía, Universidad de Valparaíso, Gran Bretana N 1111, Playa Ancha, Valparaíso, 2340000 Chile*
[9]*Infrared Processing and Analysis Center, California Institute of Technology, 1200 E. California Boulevard, Pasadena, CA 91125, USA*
[10]*Cahill Center for Astronomy and Astrophysics, California Institute of Technology, Pasadena, CA 91125, USA*
[11]*Department of Astronomy, School of Physics, Peking University, Beijing 100871, China*
[12]*Institut de Ciències del Cosmos, Universitat de Barceloa, IEEC-UB, Martí i Franquès, 1, E-08028 Barcelona, Spain*
[13]*ICREA, Pg. Lluís Companys, 23, E-08010 Barcelona, Spain*
[14]*Institute for Astronomy, 2680 Woodlawn Drive, University of Hawaii, Honolulu, HI 96822, USA*
[15]*Jet Propulsion Laboratory, California Institute of Technology, Pasadena, CA 91109, USA*

Accepted 2017 January 18. Received 2017 January 17; in original form 2016 December 2

## ABSTRACT

Mergers of galaxies are thought to cause significant gas inflows to the inner parsecs, which can activate rapid accretion on to supermassive black holes (SMBHs), giving rise to active galactic nuclei (AGN). During a significant fraction of this process, SMBHs are predicted to be enshrouded by gas and dust. Studying 52 galactic nuclei in infrared-selected local luminous and ultraluminous infrared galaxies in different merger stages in the hard X-ray band, where radiation is less affected by absorption, we find that the amount of material around SMBHs increases during the last phases of the merger. We find that the fraction of Compton-thick (CT, $N_{\rm H} \geq 10^{24}\,{\rm cm}^{-2}$) AGN in late-merger galaxies is higher ($f_{\rm CT} = 65^{+12}_{-13}$ per cent) than in local hard X-ray selected AGN ($f_{\rm CT} = 27 \pm 4$ per cent), and that obscuration reaches its maximum when the nuclei of the two merging galaxies are at a projected distance of $D_{12} \simeq 0.4$–$10.8$ kpc ($f_{\rm CT} = 77^{+13}_{-17}$ per cent). We also find that all AGN of our sample in late-merger galaxies have $N_{\rm H} > 10^{23}\,{\rm cm}^{-2}$, which implies that the obscuring material covers $95^{+4}_{-8}$ per cent of the X-ray source. These observations show that the material is most effectively funnelled from the galactic scale to the inner tens of parsecs during the late stages of galaxy mergers, and that the close environment of SMBHs in advanced mergers is richer in gas and dust with respect to that of SMBHs in isolated galaxies, and cannot be explained by the classical AGN unification model in which the torus is responsible for the obscuration.

**Key words:** galaxies: active – galaxies: nuclei – quasars: general – galaxies: Seyfert – infrared: galaxies – X-rays: general.

## 1 INTRODUCTION

Over the past 20 years, accumulated evidence shows that galaxies and the supermassive black holes (SMBHs) at their centres grow together (Ferrarese & Merritt 2000; Gebhardt et al. 2000; Kormendy & Ho 2013) during a phase in which the SMBH is accreting matter and is observed as an active galactic nucleus (AGN). It is however still uncertain how accretion on to SMBHs is triggered, since the gas and dust need to lose ∼99 per cent of their angular momentum before reaching the vicinity of the SMBH (e.g. Shlosman, Begelman & Frank 1990). The merger of two or more galaxies has been long thought to be one of the main mechanisms capable of funnelling material from the kpc- to the pc-scale environment of

★ E-mail: cricci@astro.puc.cl

SMBHs, while simultaneously triggering vigorous star formation (Sanders et al. 1988). This has been predicted by analytical studies as well as by numerical simulations (e.g. Di Matteo, Springel & Hernquist 2005), which indicate that tidal torques lead to the inflow of gas into the innermost regions (Hernquist 1989). In agreement with this idea, Treister et al. (2012) found that the fraction of AGNs in mergers increases with the AGN luminosity (see also Bessiere et al. 2012; Schawinski et al. 2012; Hickox et al. 2014; Glikman et al. 2015), and observations of optically selected (Ellison et al. 2011), IR-selected (Satyapal et al. 2014) and X-ray-selected (Silverman et al. 2011; Koss et al. 2012) samples of pairs have shown that the fraction of dual AGN is larger in systems with close companions. Studies of radio-loud AGN have also shown that galaxy interactions might play a role in triggering AGN activity (Ramos Almeida et al. 2011), as well as in the formation of strong jets (Chiaberge et al. 2015).

One of the main predictions of merger-triggered accretion is that during the final phases of a merger most of the accretion would happen when the SMBH is completely enshrouded by gas and dust (e.g. Hopkins et al. 2006). Recent studies have also shown that there seems to be an increase in the amount of obscuring material in mergers of galaxies. Studying pairs of galaxies, Satyapal et al. (2014) found that there is an enhanced fraction of IR-selected AGN with respect to optically selected AGN in advanced mergers, which suggests that a large number of objects are missed by optical classification because they are heavily obscured.

Studying galaxies at $z \sim 1$, Kocevski et al. (2015) found an increase in the fraction of galaxies undergoing mergers, or with interactions signatures, in AGN with $N_{\rm H} \geq 3 \times 10^{23}$ cm$^{-2}$ with respect to unobscured AGN. Tentative evidence of an excess of merging systems in AGN with $N_{\rm H} \geq 2 \times 10^{23}$ cm$^{-2}$ was found by Del Moro et al. (2016) studying mid-IR quasars at $z \sim 2$. Analysing the X-ray spectra of heavily obscured AGN in the COSMOS field, Lanzuisi et al. (2015) found evidence of an increase in the fraction of mergers in CT sources with respect to X-ray-selected samples. Koss et al. (2016b) also discussed a possible increase in the fraction of advanced mergers in Compton-thick (CT, $N_{\rm H} \geq 10^{24}$ cm$^{-2}$) AGN, finding that 2 out of 9 CT AGN selected by using the spectral curvature approach are in close mergers ($D_{12} < 10$ kpc). This fraction ($26^{+14}_{-12}$ per cent)[1] is higher than that typically found for *Swift*/BAT (Burst Alert Telescope) AGN ($8 \pm 2$ per cent; Koss et al. 2010).

With the aim of understanding how galaxy mergers affect the environment of AGN, we have studied a sample of 30 luminous[2] and ultraluminous[3] IR galaxies (U/LIRGs) in different merger stages (for a total of 52 individual galactic nuclei) at hard X-ray energies ($\geq$10 keV). Hard X-rays are one of the best energy bands to detect and characterize the most obscured and possibly CT AGN, due to the lower opacity of the obscuring material with respect to softer X-ray energies. The recent launch of the NASA mission *Nuclear Spectroscopic Telescope Array* (*NuSTAR*; Harrison et al. 2013), the first focusing hard X-ray (3–79 keV) telescope in orbit, has allowed the study of even some of the most obscured and elusive growth episodes of AGN (e.g. Baloković et al. 2014; Gandhi et al. 2014; Lansbury et al. 2014, 2015; Annuar et al. 2015; Brightman et al. 2015; Boorman et al. 2016; Ricci et al. 2016a,b). The objects in our sample were selected from the Great Observatories All-sky LIRG Survey (GOALS; Armus et al. 2009). GOALS is a local ($z < 0.088$) galaxy sample selected from the *Infrared Astronomical Satellite* (*IRAS*) revised bright Galaxy Survey (Sanders et al. 2003). The sample has a rich collection of ancillary data, from the radio to the X-rays (e.g. Inami et al. 2010; Iwasawa et al. 2011b; Petric et al. 2011; Romero-Cañizales et al. 2012; Díaz-Santos et al. 2013; Stierwalt et al. 2013; Privon et al. 2015, 2017), and the *IRAS* infrared selection guarantees that the sample is not biased by obscuration.

In this work, we report the results of broad-band X-ray spectroscopy for all the U/LIRGs of the sample by combining *NuSTAR* and *Swift*/BAT data with archival *Chandra*, *XMM–Newton* and *Swift*/X-ray telescope (XRT) data. From X-ray spectroscopy and multiwavelength properties, clear evidence of AGN emission is found in 25 nuclei, of which 13 are early mergers and 12 are late mergers. The X-ray spectra of these AGN were self-consistently modelled to take into account both absorption (including Compton scattering and photoelectric absorption) and reprocessing of the X-ray radiation from the circumnuclear material. This approach provides strong constraints on the line-of-sight column density. The paper is structured as follows. In Section 2, we describe the sample of galaxies used and the different merger stages, in Section 3 we report details about the X-ray data used and the data reduction, and in Section 4 we discuss the spectral fitting procedure adopted. The observed increase in the fraction of CT AGN along the merger sequence (with advanced mergers being typically more obscured than isolated galaxies) is discussed in Section 5, while in Section 6 we summarize our results and present our conclusions. In a forthcoming paper (Ricci et al. in preparation), we will discuss the relation between the multiwavelength properties of the U/LIRGs of our sample and the bolometric luminosity of the AGN. Throughout the paper, we adopt standard cosmological parameters ($H_0 = 70$ km s$^{-1}$ Mpc$^{-1}$, $\Omega_{\rm m} = 0.3$, $\Omega_{\Lambda} = 0.7$). Unless otherwise stated, all uncertainties are quoted at the 90 per cent confidence level.

## 2 SAMPLE AND MERGER STAGES

The GOALS sample contains 180 LIRGs and 22 ULIRGs selected from the *IRAS* revised bright Galaxy Sample (Sanders et al. 2003), which is a complete sample of extragalactic objects with 60 μm flux >5.24 Jy. The galaxies in GOALS represent a large, statistically complete sample of U/LIRGs. Objects in GOALS have been observed by *Spitzer* and *Herschel* (Inami et al. 2010, 2013; Díaz-Santos et al. 2011, 2013, 2014; Petric et al. 2011; Stierwalt et al. 2013, 2014). Our sample contains all GOALS sources observed by *NuSTAR* and for which data were available as of 2016 March. This includes: i) sources located at <120 Mpc, and with $\log(L_{\rm IR}/L_{\odot}) > 11.3$, amongst which ten LIRGs in different merger stages that were awarded to our group during AO–1 (for a total of 200 ks, PI: F. E. Bauer); ii) the nearest ($z < 0.078$) ULIRGs from Sanders et al. (2003) (see Teng et al. 2015 for details); iii) sources detected by *Swift*/BAT and observed as a part of the campaign aimed at characterising local hard X-ray selected sources with *NuSTAR*. We excluded the four U/LIRGs classified as non-mergers (*N* stage) by Stierwalt et al. (2013) since we are interested in studying the evolution of obscuration along the merger sequence. We also included three systems (IRAS F23007+0836, IRAS 23262+0314, IRAS F13197−1627) that were detected at hard X-rays by *Swift*/BAT (Baumgartner et al. 2013) but have not been observed by *NuSTAR*, to avoid any possible bias in the *NuSTAR* selection of BAT sources.

[1] The value was calculated following Cameron et al. (2012), and the uncertainties represent the 16th and 84th quantiles of a binomial distribution.
[2] $L_{\rm IR}(8-1000\ \mu{\rm m}) = 10^{11}-10^{12}\ {\rm L}_{\odot}$.
[3] $L_{\rm IR}(8-1000\ \mu{\rm m}) > 10^{12}\ {\rm L}_{\odot}$.

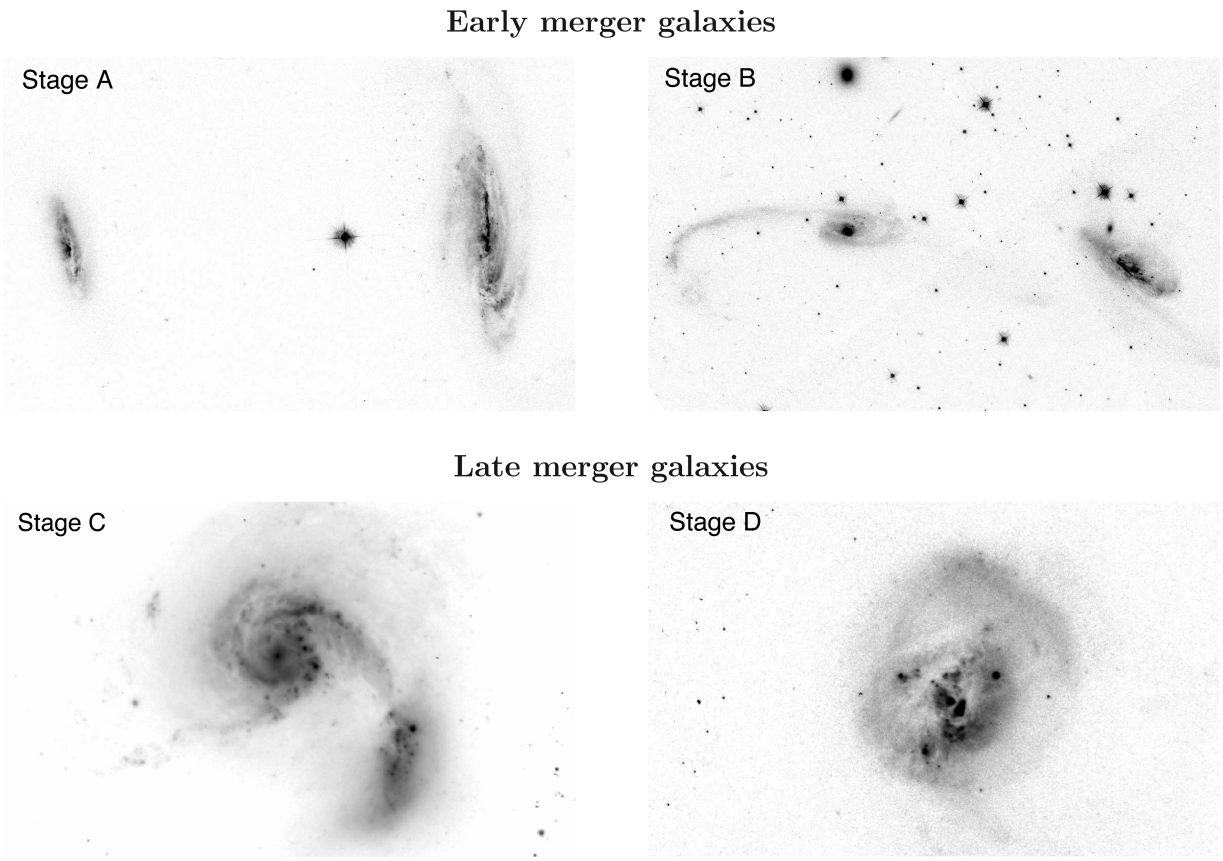


**Figure 1.** Merger stages of U/LIRGs from the GOALS sample. *HST* images of four systems in different merger stages: IRAS F11231+1456 (stage A, *F*435*W*), ESO 069−IG006 (stage B, *F*435*W*), NGC 6090 (stage C, *F*814*N*) and IRAS F23365+3604 (stage D, *F*435*W*). Objects in stage A and B are *early mergers* while those in stage C and D are *late mergers* (see Section 2).

We divided GOALS galaxies into four subsamples, based on the merger stage determined by Stierwalt et al. (2013) and Haan et al. (2011) from visual inspection of *Spitzer* IRAC 3.6 μm and *Hubble Space Telescope* (*HST*) images (see Fig. 1 and Table 1). The merger sequence we considered is the following:

**Stage A** are systems in pre-merger, i.e. galaxy pairs prior to a first encounter.

**Stage B** are objects in the initial phases of merger, i.e. galaxies after the first encounter, with galaxy discs still symmetric and showing signs of tidal tails.

**Stage C** are systems in the mid-stage of merger, showing amorphous discs, tidal tails and other signs of merger activity.

**Stage D** are sources in the final merger stages, showing the two nuclei in a common envelope or only a single nucleus.

Objects in stage A and B can be considered *early mergers*, and those in stage C and D *late mergers*. We used the merger classifications provided by Stierwalt et al. (2013), with the exception of the following three systems.

(i) IRAS F14544−4255 (IC 4518A and IC 4518B) is in the GOALS sample but, while *Spitzer* imaging is available, this system was not classified by Stierwalt et al. (2013). Optical and IR images show that the two galaxies are clearly separated (36 arcsec or 12.0 kpc) and show signs of tidal interactions (see Appendix A21). They were therefore classified as being in stage B.

(ii) IRAS F18293−3413 is classified as being in stage C by Stierwalt et al. (2013). *HST* imaging (Fig. 2) shows, however, that the two systems do not share a common envelope, and the source was classified as being in a pre-merger stage by Haan et al. (2011). Given the much smaller size of the companion object, we reclassify this object as stage N.

(iii) IRAS F21453−3511 (NGC 7130), which was initially classified as a non-merger, has been recently shown to present post-merger features by Davies et al. (2014). We therefore reclassify this source as stage D with a single nucleus.

Overall our sample consists of 30 systems, of which 8 show a single nucleus and the remaining 22 show two nuclei, for a total of 52 galactic nuclei. Our sample is a representative subsample of GOALS galaxies. The histogram of the 8–1000 μm luminosities ($L_{\rm IR}$) of all objects in the GOALS sample and of the GOALS galaxies in our sample are showed in the top panel of Fig. 3 (blue and red lines, respectively). The two samples have similar luminosities, and performing a Kolmogorov–Smirnov (KS) test we find a p-value of 0.13, which implies that our sample does not have a distribution of $L_{\rm IR}$ significantly different from that of the GOALS sample. Similarly, the distribution of distances of our sample does not differ from that of GOALS galaxies (bottom panel of Fig. 3), and the KS test results in a p-value of 0.91. The two panels of Fig. 3 also show the distributions of the AGN in our sample (black lines). A KS test between the luminosity (distance) distributions of AGN and of all the galaxies in the GOALS sample shows that the two samples are not significantly different, resulting in a p-value of 0.16 (0.60).

The sample objects, together with their merger stage and the distance between the two nuclei are reported in Table 1. The images of the objects of our samples are shown in Figs 4–8. *NuSTAR* observations of 15 systems have been studied before, and for these objects we report the results from the literature in Table 2.

**Table 1.** Sample used for our work. The table shows (1) the IRAS name of the source, (2) the counterparts, (3) the redshift, (4) the merger stage and (5) the separation between the two nuclei in arcsec and (6) in kpc. In (5) and (6), we report 'S' for objects for which a single nucleus is observed.

| (1) IRAS name | (2) Source | (3) $z$ | (4) M | (5) $D_{12}$ (arcsec) | (6) $D_{12}$ (kpc) |
|---|---|---|---|---|---|
| F00085−1223 | NGC 34 | 0.019617 | D | S | S |
| F00163−1039 | Arp 256 & MCG−02 − 01 −052 | 0.027152 | B | 56.1 | 33.1 |
| F00506+7248 | MCG+12−02 −001 | 0.015698 | C | 0.9 | 0.3 |
| F02069−1022 | NGC 833 & NGC 835 | 0.012889 | A | 55.9 | 15.7 |
| F05054+1718 | CGCG 468−002E & CGCG 468−002W | 0.018193 | B | 29.6 | 11.3 |
| F05189−2524 | IRAS 05189−2524 | 0.042563 | D | S | S |
| F08572+3915 | IRAS 08572+3915 (NW & SE) | 0.058350 | D | 4.4 | 5.6 |
| F09320+6134 | UGC 05101 | 0.039367 | D | S | S |
| F09333+4841 | MCG+08−18 −013 & MCG+08−18 −012 | 0.025941 | A | 66.5 | 35.4 |
| F10015−0614 | NGC 3110 & MCG−01 − 26 −013 | 0.016858 | A | 108.9 | 37.7 |
| F10257−4339 | NGC 3256 | 0.009354 | D | 5.1 | 1.0 |
| F10565+2448 | IRAS 10565+2448 | 0.043100 | D | 7.4 | 6.7 |
| F11257+5850 | Arp 299 (NGC3690W & NGC3690E) | 0.010220 | C | 21.3 | 4.6 |
| F12043−3140 | ESO 440−IG058N & ESO 440−IG058S | 0.023413 | B | 12.0 | 5.9 |
| F12540+5708 | Mrk 231 | 0.042170 | D | S | S |
| F12590+2934 | NGC 4922N & NGC 4922S | 0.023169 | C | 21.2 | 10.8 |
| 13120−5453 | IRAS 13120−5453 | 0.030761 | D | S | S |
| F13197−1627 | MCG−03 − 34 −064 & MCG−03 − 34 −063 | 0.021328 | A | 106.2 | 37.7 |
| F13428+5608 | Mrk 273 | 0.037780 | D | 0.9 | 0.7 |
| F14378−3651 | IRAS 14378−3651 | 0.067637 | D | S | S |
| F14544−4255 | IC 4518A & IC 4518B | 0.016261 | B | 36.0 | 12.0 |
| F15327+2340 | Arp 220W & Arp 220E | 0.018126 | D | 1.0 | 0.4 |
| F16504+0228 | NGC 6240N & NGC 6240S | 0.024480 | D | 1.4 | 0.7 |
| F16577+5900 | NGC 6286 & NGC 6285 | 0.018349 | B | 91.1 | 35.8 |
| F17138−1017 | IRAS F17138−1017 | 0.017335 | D | S | S |
| 20264+2533 | MCG +04 − 48 −002 & NGC 6921 | 0.013900 | A | 91.4 | 27.1 |
| F21453−3511 | NGC 7130 | 0.016151 | D | S | S |
| F23007+0836 | NGC 7469 & IC 5283 | 0.016317 | A | 79.7 | 26.8 |
| F23254+0830 | NGC 7674 & NGC 7674A | 0.028924 | A | 34.1 | 20.7 |
| 23262+0314 | NGC 7679 & NGC 7682 | 0.017139 | A | 269.7 | 97.3 |

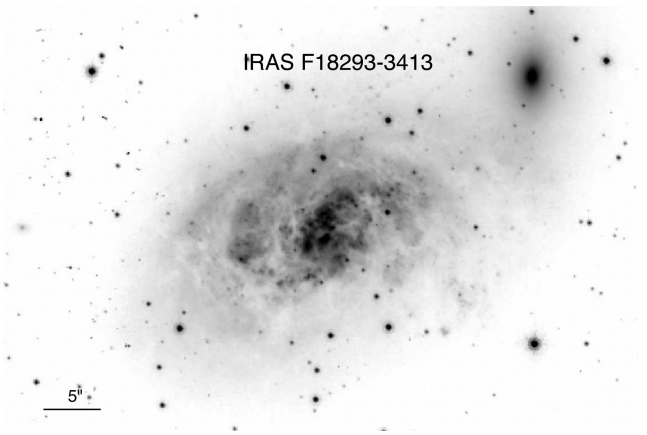


**Figure 2.** *HST* image of IRAS F18293−3413 (*HST F*814*W*; 5 arcsec ≃ 1.8 kpc).

## 3 X-RAY OBSERVATIONS AND DATA REDUCTION

We analysed the X-ray observations of 16 systems, using *XMM–Newton* (Section 3.2), *Chandra* (Section 3.3), *NuSTAR* (Section 3.1), *Swift*/BAT and *Swift*/XRT data (Section 3.4). The observation log of our sample is reported in Table 3. Details about the analysis of all sources are reported in Appendix A. The angular separation between the nuclei and the relation with the extraction regions used for the different instruments are discussed in detail in Appendix A for every source analysed here.

### 3.1 *NuSTAR*

We studied here the 13 observations carried out by the *NuSTAR* (Harrison et al. 2013) not studied before. Of these, nine were observed as a part of a dedicated campaign awarded to our group during *NuSTAR* AO-1 (PI F. Bauer). The *NuSTAR* data were processed using the *NuSTAR* Data Analysis Software NUSTARDAS v1.4.1 within HEASOFT v6.16, adopting the calibration files released on UT 2015 March 16 (Madsen et al. 2015). A circular region of 45 arcsec was used for the sources, while the background was extracted from an annulus centred on the X-ray source, with an inner and outer radius of 50 and 100 arcsec, respectively. In none of the *NuSTAR* observations analysed here are two AGN confused or within the same extraction region. This is due to the fact that (i) no nucleus was detected by *NuSTAR*; (ii) one nucleus only was detectable by *NuSTAR*; (iii) if both nuclei were detectable, they were at a distance sufficient to avoid confusion.

### 3.2 *XMM–Newton*

*XMM–Newton* (Jansen et al. 2001) observations of seven systems of our sample were available. We analysed EPIC/PN (Strüder et al. 2001) and MOS (Turner et al. 2001) data by reducing the original data files using *XMM–Newton* Standard Analysis Software

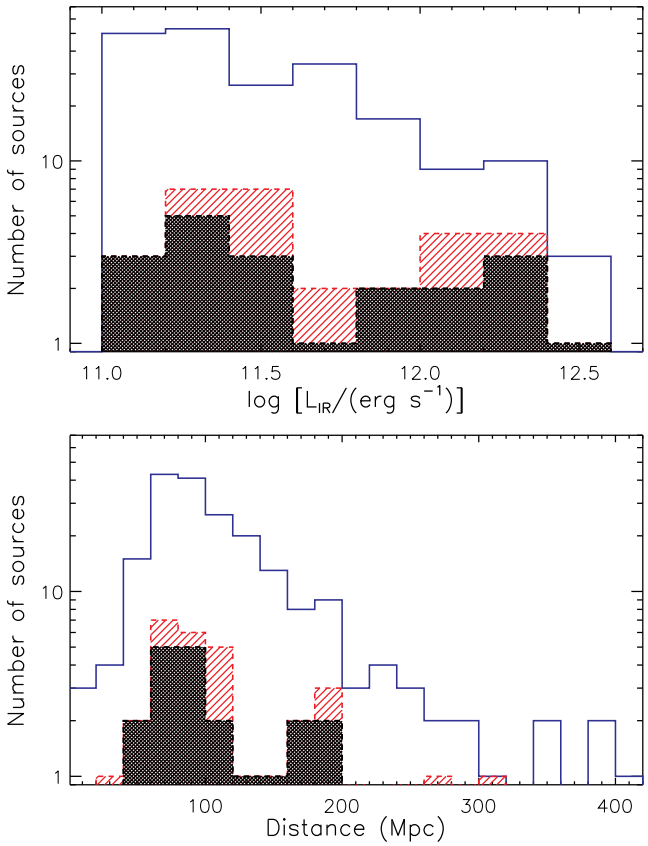


**Figure 3.** Top panel: histogram of the 8–1000 μm luminosity ($L_{\rm IR}$) of all the systems in the GOALS sample (blue empty histogram), of the GOALS objects in our sample (red histogram) and of the AGN in our sample (black filled histogram). Bottom panel: same as top panel for the distances.

(SAS) version 12.5.0 (Gabriel et al. 2004). The raw PN and MOS data files were then reduced using the `epchain` and `emchain` tasks, respectively.

The observations were then filtered for periods of high background activity by analysing the EPIC/PN and MOS background light curves in the 10–12 keV band and above 10 keV, respectively. For both cameras, we extracted the spectra of the sources using a circular region of 25 arcsec radius, while the background was extracted from a circular region of 40 arcsec radius, located on the same CCD of the source and in a zone where no other source was found.

For all the *XMM–Newton* observations analysed here, with the exception of IRAS F14544−4255, the two nuclei are at a distance larger than the size of the extraction region used. In the case of IRAS F14544−4255, the two galaxies are separated by ∼36 arcsec from each other, and we used a radius of 5 arcsec (20 arcsec) for the spectral extraction of IC 4518B (IC 4518A).

### 3.3 *Chandra*

*Chandra* (Weisskopf et al. 2000) ACIS (Garmire et al. 2003) observations are available for 10 sources in our sample. Most of these observations were carried out as a part of the campaign aimed at following up GOALS sources (PI: D. Sanders, see Iwasawa et al. 2011b and Torres Albà et al. in preparation for details). We reduced *Chandra* ACIS data following standard procedures, using CIAO v.4.6. All data were reprocessed using the CHANDRA_REPRO task. For the extraction we used a circular region with a radius of 10 arcsec, which included all the X-ray emission associated with the objects. A circular region with the same radius, selected in region where no other source was detected was used for the background.

### 3.4 *Swift* XRT and BAT

Data from the XRT (Burrows et al. 2005) on board *Swift* were used only for IRAS F05054+1718. *Swift*/XRT data analysis was performed using the XRTPIPELINEV0.13.0 within HEASOFT V6.16 following the standard guidelines. *Swift*/BAT time-averaged spectra were used for two systems (IRAS F23007+0836 and IRAS F13197−1627), and were taken from the latest release of the *Swift*/BAT catalogue (Baumgartner et al. 2013).

## 4 X-RAY SPECTRAL ANALYSIS

The X-ray spectral analysis was carried out within XSPEC v.12.8.2 (Arnaud 1996). Galactic absorption in the direction of the source was added to all models using the Tuebingen–Boulder interstellar matter absorption model TBABS (Wilms, Allen & McCray 2000), fixing the column density ($N_{\rm H}^{\rm Gal}$) to the value reported by Kalberla et al. (2005) for the coordinates of the source. Abundances were fixed to solar values. Spectra were typically rebinned to 20 counts per bin in order to use $\chi^2$ statistics. Cash statistics (Cash 1979) were used to fit *Chandra* spectra, and the source spectra were binned to have one count per bin, in order to avoid issues related to empty bins in XSPEC.

We used a variety of spectral models to reproduce the X-ray emission from the galaxies in our sample. To model the underlying stellar processes, which can lead to X-ray emission in U/LIRGs, we used a thermal plasma (APEC in XSPEC) and a power-law component (ZPOWERLAW), which reproduce X-ray emission from hot plasma gas and an underlying population of X-ray binaries, respectively. The free parameters of the APEC model are the temperature ($kT$) and the normalization ($n_{\rm apec}$), while for the power-law component they are the photon index ($\Gamma$) and the normalization ($n_{\rm po}$). If required by the data, we added photoelectric absorption (ZPHABS) to the thermal plasma and the X-ray binary emission. The only free parameter of this component is the column density ($N_{\rm H}^{\rm SF}$).

From X-ray spectroscopy and multiwavelength properties evidence of AGN emission is found in 25 nuclei, of which 13 are early mergers and 12 are late mergers. While we cannot completely exclude the presence of low-luminosity or heavily obscured AGN in the systems for which no evidence of AGN activity is found, the X-ray spectra of all the sources analysed here (with the exception of IRAS F17138−1017) have characteristics consistent with those of star-forming regions in the X-ray band. We refer the reader to Appendix A for a detailed discussion on the presence of accreting SMBHs and on the X-ray and multiwavelength properties of all sources of our sample.

In order to self-consistently reproduce absorbed and reprocessed X-ray radiation from the circumnuclear material of the AGN, we used the torus model developed by Brightman & Nandra (2011), which considers an X-ray source surrounded by a spherical-toroidal structure (ATABLE{TORUS1006.FITS}). This model was developed from ray-tracing simulations and reproduces the main

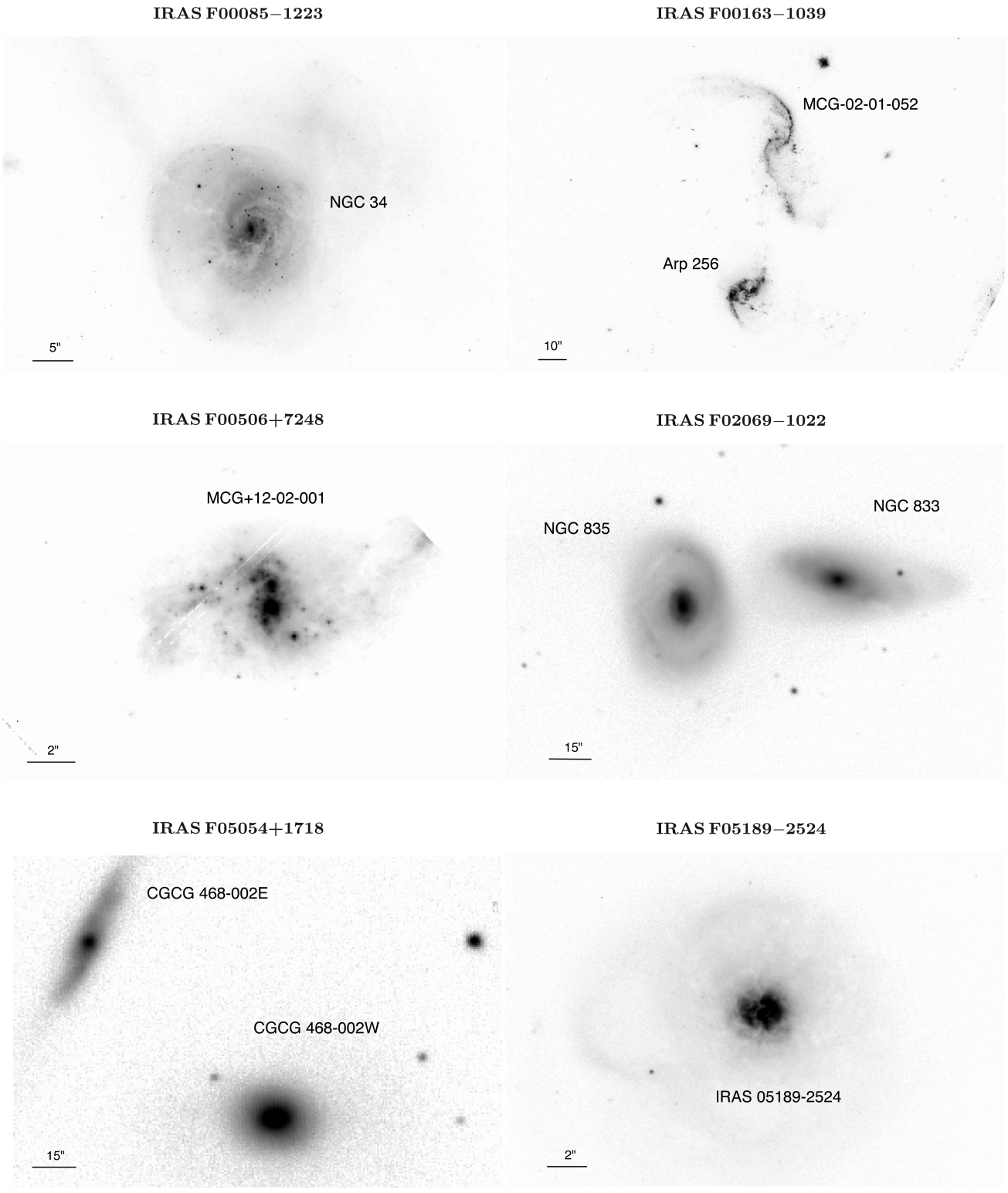


**Figure 4.** Fields around IRAS F00085−1223 (*HST F*435*W*; 5 arcsec ≃ 1.9 kpc), IRAS F00163−1039 (*HST F*435*W*; 10 arcsec ≃ 5.9 kpc), IRAS F00506+7248 (*HST F*110*W*; 2 arcsec ≃ 0.7 kpc), IRAS F02069−1022 (SDSS *r* band; 15 arcsec ≃ 4.2 kpc), IRAS F05054+1718 (UKIDSS *K* band; 15 arcsec ≃ 5.7 kpc), IRAS F05189−2524 (*HST F*435*W*; 2 arcsec ≃ 1.8 kpc). In all images, north is to the top and east is to the left.

features arising from the reprocessing of the primary X-ray radiation from neutral material (e.g. Matt, Perola & Piro 1991; Murphy & Yaqoob 2009): a narrow Fe K$\alpha$ line at 6.4 keV (e.g. Shu, Yaqoob & Wang 2010; Ricci et al. 2014) and the Compton hump at ∼20–30 keV (e.g. Koss et al. 2016b). These features are particularly prominent in CT AGN, due to the fact that most of the primary X-ray emission is obscured. The free parameters of the torus model we used here are the column density ($N_{\rm H}$), the photon index ($\Gamma$) and

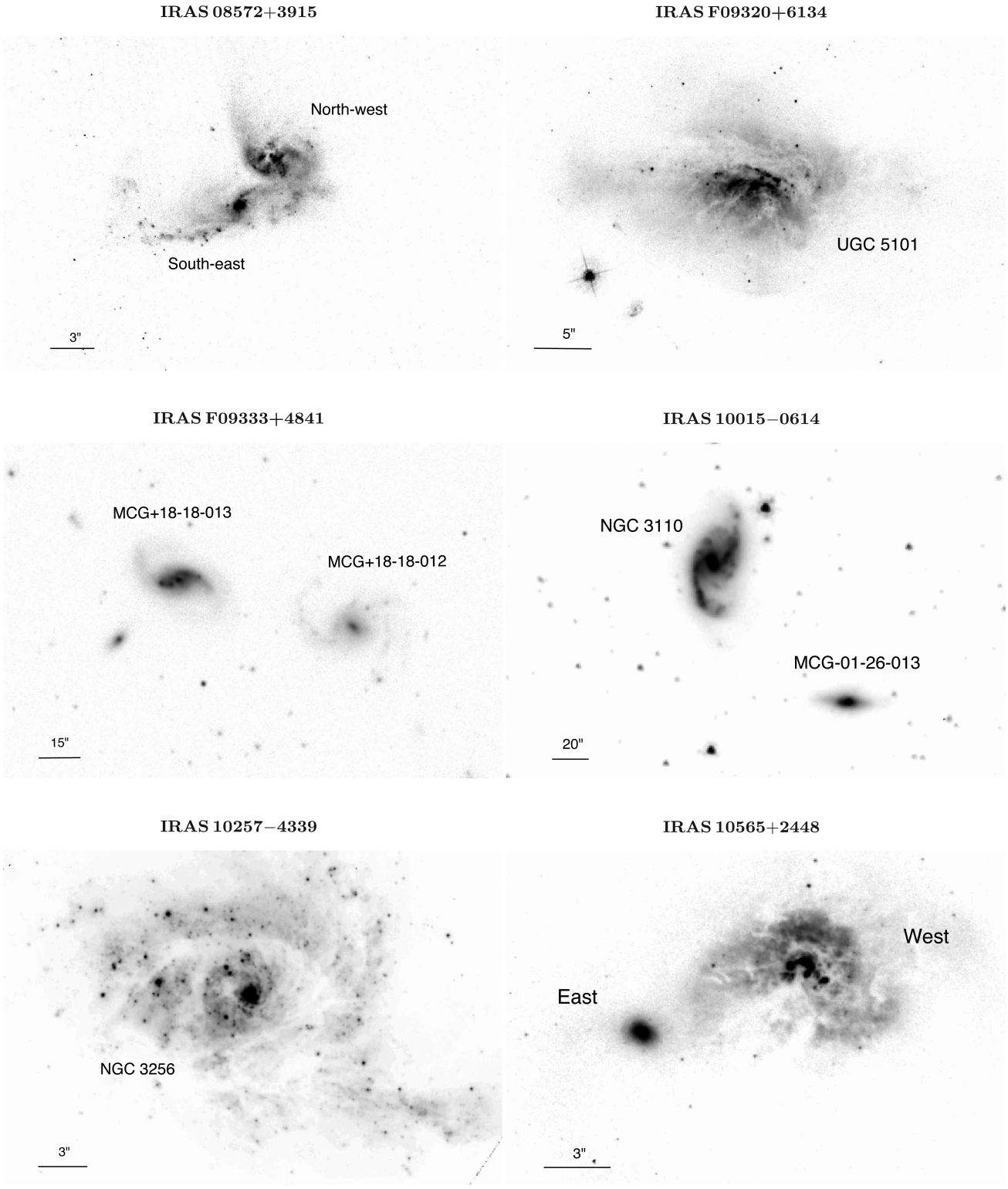


**Figure 5.** Fields around IRAS 08572+3915 (*HST F*435*W*; 3 arcsec ≃ 3.8 kpc), IRAS F09320+6134 (*HST F*435*W*; 5 arcsec ≃ 4.1 kpc), IRAS F09333+4841 (SDSS *r* band; 15 arcsec ≃ 8.0 kpc), IRAS F10015−0614 (*Spitzer*/IRAC 3.6 μm; 20 arcsec ≃ 6.9 kpc), IRAS 10257−4339 (*HST F*814*W*; 3 arcsec ≃ 0.6 kpc), and IRAS 10565+2448 (*HST F*435*W*; 3 arcsec ≃ 2.7 kpc). In all images, north is to the top and east is to the left.

the normalization ($n$) of the primary X-ray emission. In this model, $N_{\rm H}$ does not vary with the inclination angle, which we set to the maximum value permitted ($\theta_{\rm i} = 87.1$ deg). The model allows also to vary the half-opening angle of the torus ($\theta_{\rm OA}$). This component was fixed to $\theta_{\rm OA} = 60$ deg whenever it could not be constrained. In obscured AGN, a second, unabsorbed, power-law component is often observed emerging at energies lower than the photoelectric cutoff. This component has often been associated with Thomson

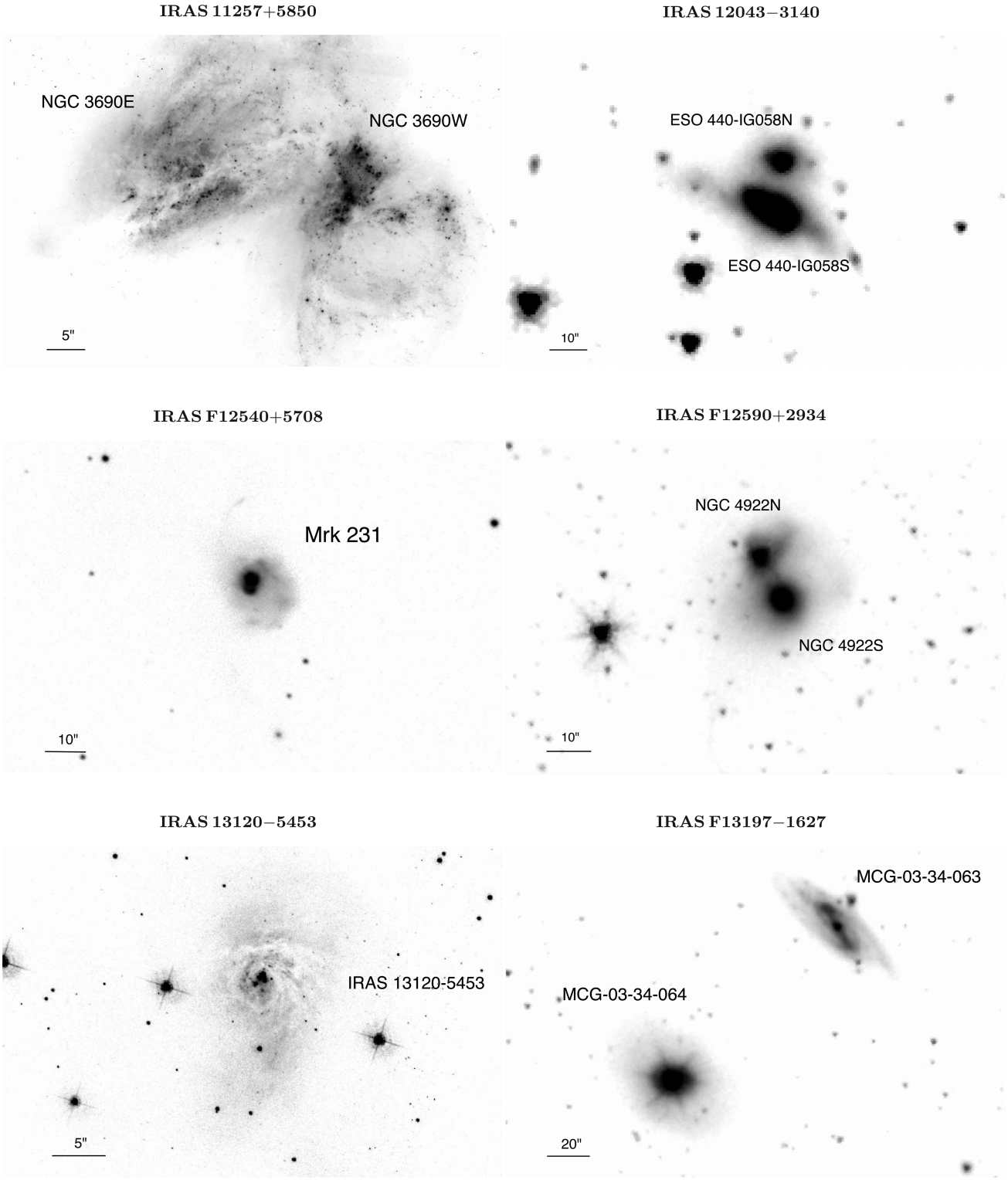


**Figure 6.** Fields around IRAS 11257+5850 (*HST F435W*; 5 arcsec $\simeq$ 1.1 kpc), IRAS 12043−3140 (*Spitzer*/IRAC 3.6 μm; 10 arcsec $\simeq$ 4.9 kpc), IRAS F12540+5708 (SDSS *g* band; 10 arcsec $\simeq$ 8.8 kpc), IRAS F12590+2934 (*Spitzer*/IRAC 3.6 μm; 10 arcsec $\simeq$ 5.1 kpc), IRAS 13120−5453 (*HST F435W*; 5 arcsec $\simeq$ 3.2 kpc) and IRAS F13197−1627 (*Spitzer*/IRAC 3.6 μm; 20 arcsec $\simeq$ 7.1 kpc). In all images, north is to the top and east is to the left.

scattering of the primary X-ray radiation from ionized gas (e.g. Ueda et al. 2007). To take into account this feature, which could be confused with the emission arising from a population of X-ray binaries, when an AGN is present we fixed the photon index of the second power-law component to the value of the AGN primary X-ray emission. The amount of scattered radiation is parametrized in terms of $f_{\rm scatt}$, which is the ratio between the normalizations of the scattered component and of the primary X-ray emission.

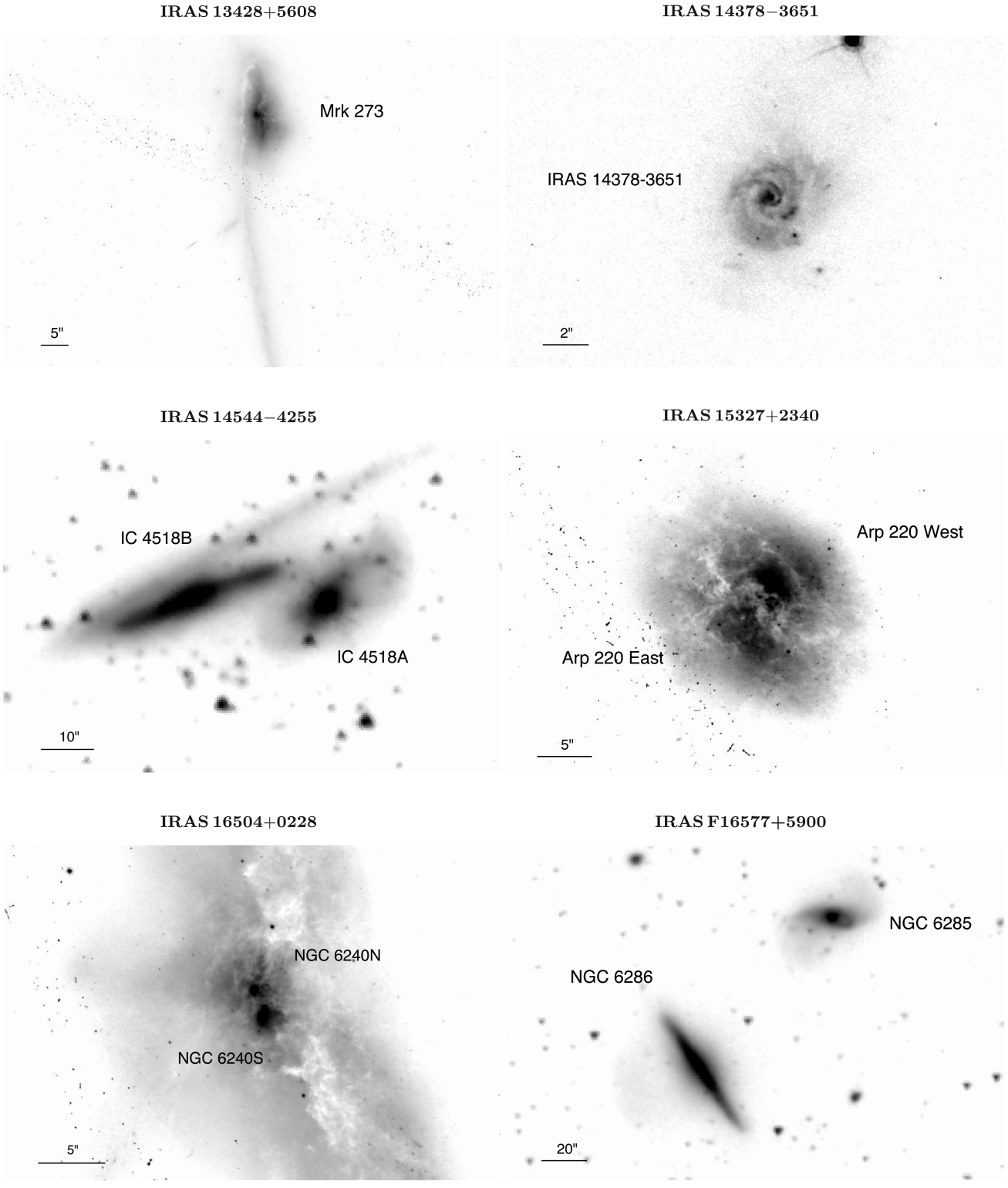


**Figure 7.** Fields around IRAS 13428+5608 (*HST F*814*W*; 5 arcsec ≃ 3.9 kpc), IRAS 14378−3651 (*HST F*435*W*; 2 arcsec ≃ 2.9 kpc), IRAS 14544−4255 (*Spitzer*/IRAC 3.6 μm; 10 arcsec ≃ 3.3 kpc), IRAS 15327+2340 (*HST F*814*W*; 5 arcsec ≃ 2 kpc), IRAS 16504+0228 (*HST F*814*W*; 5 arcsec ≃ 2.5 kpc), IRAS F16577+5900 (*Spitzer*/IRAC 3.6 μm; 20 arcsec ≃ 7.9 kpc). In all images, north is to the top and east is to the left.

The results obtained by our spectral analysis are summarized in Table 4. Details about the spectral fitting and the multiwavelength properties of the galaxies of our sample are reported in Appendix A, while the X-ray spectra are illustrated in Appendix B.

## 5 DISCUSSION

The broad-band X-ray spectral analysis of the objects in our sample shows that AGN in advanced merger stages are typically more obscured than AGN in isolated galaxies or in galaxies in the early

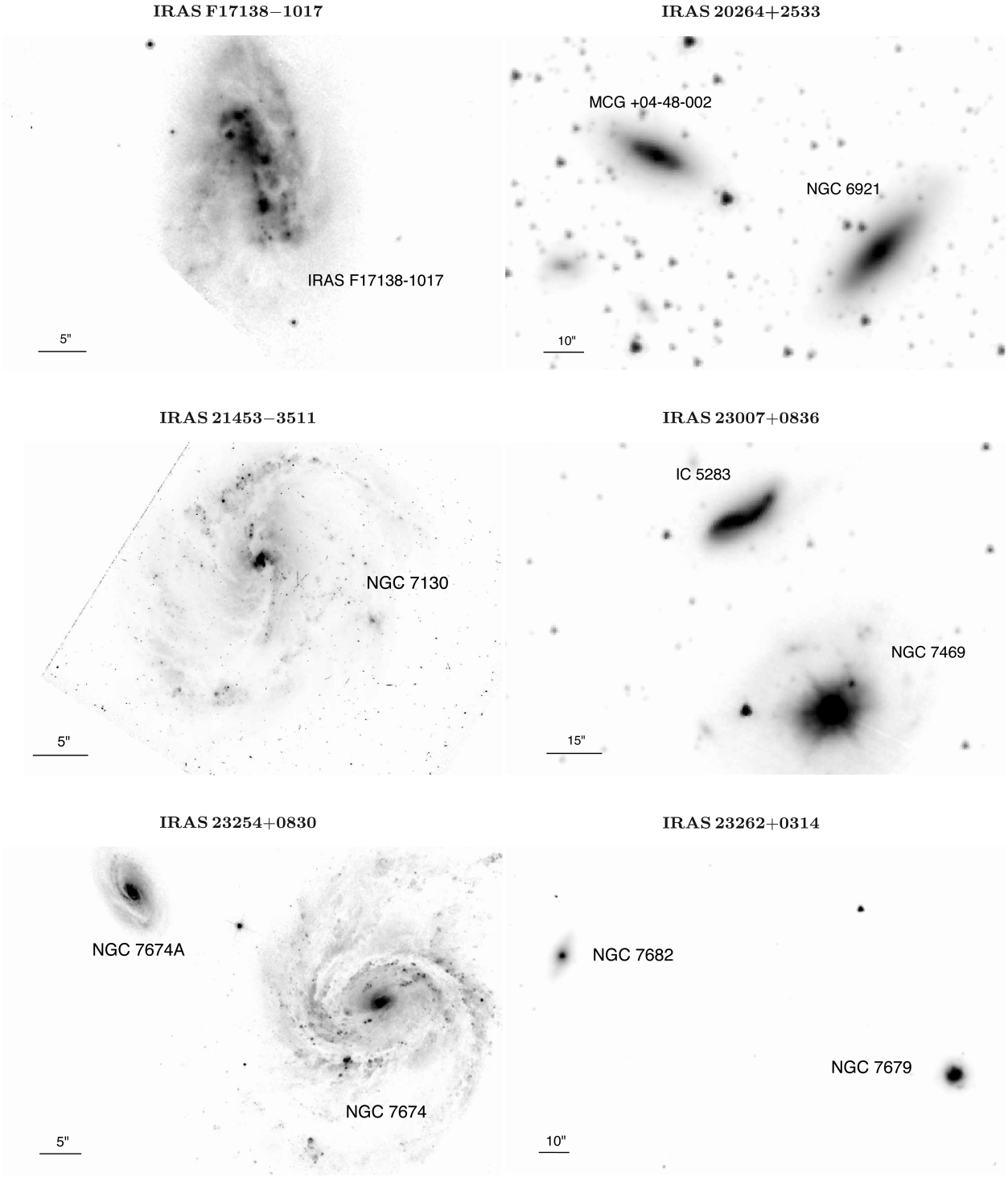


**Figure 8.** Fields around IRAS F17138−1017 (*HST F110W*; 5 arcsec ≃ 1.8 kpc), IRAS 20264+2533 (*Spitzer*/IRAC 3.6 μm; 10 arcsec ≃ 3.0 kpc), IRAS 21453−3511 (*HST F606W*; 5 arcsec ≃ 1.5 kpc), IRAS 23007+0836 (*Spitzer*/IRAC 3.6 μm; 15 arcsec ≃ 5.0 kpc), IRAS 23254+0830 (*HST F435W*; 5 arcsec ≃ 3.0 kpc) and IRAS 23262+0314 (*Spitzer*/IRAC 3.6 μm; 10 arcsec ≃ 3.6 kpc). In all images, north is to the top and east is to the left.

stages of mergers (Fig. 9). In Fig. 10, we illustrate the average normalized spectral models of AGN in galaxies in early (red continuous line) and late (black dashed line) merger stage. The image clearly illustrates that the main features indicating heavy obscuration, the Fe K$\alpha$ line and Compton hump, are stronger in AGN in late-merger stage galaxies. We find that AGN in late-merger stage galaxies host a significantly (99 per cent confidence) larger fraction of CT AGN ($65^{+12}_{-13}$ per cent) compared to local hard X-ray selected AGN (27 ± 4 per cent, Ricci et al. 2015; see also Burlon et al. 2011), which are mostly found in non-merging systems.[4] The

[4] Only 8 ± 2 per cent of *Swift*/BAT AGN are found in close mergers (Koss et al. 2010).

**Table 2.** The table reports (1) the IRAS name, (2) the counterparts, (3) the values of the column density in the direction of the AGN reported in the literature and (4) the reference for $N_{\rm H}$.

| (1) IRAS name | (2) Source | (3) $N_{\rm H}$ ($10^{22}$ cm$^{-2}$) | (4) Reference |
|---|---|---|---|
| F02069−1022 | NGC 833 | $28 \pm 3$ | Oda et al. (in preparation) |
| | NGC 835[a] | $55^{+15}_{-10}$ | Oda et al. (in preparation) |
| | NGC 835[b] | $30 \pm 2$ | Oda et al. (in preparation) |
| F05189−2524 | IRAS 05189−2524 | $12.7^{+1.0}_{-0.7}$ | Teng et al. (2015) |
| F08572+3915 | IRAS 08572+3915 | – | Teng et al. (2015) |
| F09320+6134 | UGC 5101 | $132^{+32}_{-37}$ | Oda et al. (2017) |
| F10257−4339 | NGC 3256 | – | Lehmer et al. (2015) |
| F10565+2448 | IRAS 10565+2448 | – | Teng et al. (2015) |
| F11257+5850 | NGC 3690W | $350^{NC}_{-20}$ | Ptak et al. (2015) |
| F12540+5708 | Mrk 231 | $14.5^{+3.1}_{-2.4}$ | Teng et al. (2014) |
| 13120−5453 | IRAS 13120−5453 | $316^{+233}_{-129}$ | Teng et al. (2015) |
| F13428+5608 | Mrk 273 | $44^{+10}_{-6}$ | Teng et al. (2015) |
| F14378−3651 | IRAS 14378−3651 | – | Teng et al. (2015) |
| F15327+2340 | Arp 220W | $\geq$530 | Teng et al. (2015) |
| F16504+0228 | NGC 6240N | $155^{+72}_{-23}$ | Puccetti et al. (2016) |
| | NGC 6240S | $147^{+21}_{-17}$ | Puccetti et al. (2016) |
| F16577+5900 | NGC 6286 | $111^{+109}_{-41}$ | Ricci et al. (2016a) |
| F23254+0830 | NGC 7674 | $\gtrsim$300 | Gandhi et al. (2016) |

*Notes*. NC: value not constrained; [a]*XMM–Newton* observation; [b]*NuSTAR* and *Chandra* observation.

**Table 3.** X-ray observations log. The columns report (1) the IRAS name of the source, (2) the counterparts, (3) the X-ray facility, (4) the observation ID and (5) the exposure time. For *XMM–Newton*, the exposures listed are those of EPIC/PN, MOS1 and MOS2, while for *NuSTAR* those of FPMA and FPMB.

| (1) IRAS name | (2) Source | (3) Facility | (4) Observation ID | (5) Exposure (ks) |
|---|---|---|---|---|
| F00085−1223 | NGC 34 | *NuSTAR* | 60101068002 | 21.4/21.4 |
| | | *Chandra* | 15061 | 14.8 |
| | | *XMM–Newton* | 0150480501 | 12.0/16.7/17.2 |
| F00163−1039 | Arp 256 & MCG−02 − 01 −052 | *NuSTAR* | 60101069002 | 20.5/20.5 |
| | | *Chandra* | 13823 | 29.6 |
| F00506+7248 | MCG+12−02 −001 | *NuSTAR* | 60101070002 | 25.5/25.5 |
| | | *Chandra* | 15062 | 14.3 |
| F05054+1718 | CGCG 468−002E & CGCG 468−002W | *NuSTAR* | 60006011002 | 15.5/15.5 |
| | | *Swift*/XRT | 49706 | 72.1 |
| F09333+4841 | MCG+08−18 −013 & MCG+08−18 −012 | *NuSTAR* | 60101071002 | 19.1/19.1 |
| | | *Chandra* | 15067 | 13.8 |
| F10015−0614 | NGC 3110 & MCG−01 − 26 −013 | *NuSTAR* | 60101072002 | 17.9/17.8 |
| | | *Chandra* | 15069 | 14.9 |
| | | *XMM–Newton* | 0550460201 | 11.0/17.8/18.0 |
| F12043−3140 | ESO 440−IG058N & ESO 440−IG058S | *NuSTAR* | 60101073002 | 28.6/28.6 |
| | | *Chandra* | 15064 | 14.8 |
| F12590+2934 | NGC 4922N & NGC 4922S | *NuSTAR* | 60101074002 | 20.7/20.6 |
| | | *Chandra* | 15065 | 14.9 |
| F13197−1627 | MCG−03 − 34 −064 & MCG−03 − 34 −063 | *XMM–Newton* | 0506340101 | 66.5/85.4/85.9 |
| F14544−4255 | IC 4518A & IC 4518B | *NuSTAR* | 60061260002 | 7.8/7.8 |
| | | *XMM–Newton* | 0406410101 | 21.2/24.4 |
| F16577+5900 | NGC 6286 & NGC 6285 | *NuSTAR* | 60101075002 | 17.5/17.5 |
| | | *Chandra* | 10566 | 14.0 |
| F17138−1017 | IRAS F17138−1017 | *NuSTAR* | 60101076002 | 25.9/25.9 |
| | | *Chandra* | 15063 | 14.8 |
| 20264+2533 | MCG +04−48 −002 & NGC 6921 | *NuSTAR* | 60061300002 | 19.5/19.5 |
| | | *XMM–Newton* | 0312192301 | 6.5/12.4/12.7 |
| F21453−3511 | NGC 7130 | *NuSTAR* | 60061347002 | 21.2/21.2 |
| | | *Chandra* | 2188 | 38.6 |
| F23007+0836 | NGC 7469 & IC 5283 | *XMM–Newton* | 0207090101 | 59.2 |
| 23262+0314 | NGC 7679 & NGC 7682 | *XMM–Newton* | 0301150501 | 13.1/19.3/19.1 |

**Table 4.** The table reports the values obtained from the X-ray spectral analysis of the sources of our sample. For each source we list (1) the IRAS name of the source, (2) the counterparts, (3) the column density of X-ray emission related to star formation, (4) the temperature of the collisionally ionized plasma, (5) the photon index of the soft X-ray emission due to X-ray binaries or to the scattered emission from the AGN, (6) the column density and (7) the photon index of the AGN, and (8) the value of the Cash [C] or $\chi^2$ statistics and the number of degrees of freedom (DOF). Objects in which both statistics were used to fit different spectra are reported as [C/$\chi^2$], and the value of the statistic is the combination of the two.

| (1) IRAS name | (2) Source | (3) $N_{\rm H}^{\rm SF}$ ($10^{21}$ cm$^{-2}$) | (4) $kT$ (keV) | (5) $\Gamma_{\rm bin.}$ | (6) $N_{\rm H}$ ($10^{22}$ cm$^{-2}$) | (7) $\Gamma$ | (8) $\chi^2$/DOF |
|---|---|---|---|---|---|---|---|
| F00085−1223 | NGC 34 | – | $0.78^{+0.07}_{-0.08}$ | 1.57[a] | $53 \pm 11$ | $1.57^{+0.12}_{-0.14}$ | 240.7/288 [C/$\chi^2$] |
| F00163−1039 | Arp 256 | $3.4^{+2.4}_{-2.3}$ | $0.30^{+0.45}_{-0.10}$ | $2.47^{+0.38}_{-0.32}$ | – | – | 167.9/191 [C] |
| | MCG−02 − 01 −052 | – | $0.61 \pm 0.27$ | $1.93^{+0.56}_{-0.60}$ | – | – | 62.0/91 [C] |
| F00506+7248 | MCG+12−02 −001 | $5.4^{+2.4}_{-2.0}$ | – | $3.07^{+0.57}_{-0.49}$ | – | – | 131.8/144 [C] |
| F05054+1718 | CGCG 468−002W | – | – | – | $1.50 \pm 0.09$ | $1.69 \pm 0.04$ | 604.0/545 [$\chi^2$] |
| F09333+4841 | MCG+08−18 −013 | $3.0^{+2.6}_{-2.1}$ | – | $2.26^{+0.27}_{-0.21}$ | – | – | 57.6/71 [C] |
| F10015−0614 | NGC 3110 | $0.7 \pm 0.4$ | $0.63^{+0.10}_{-0.06}$ | $2.18^{+0.27}_{-0.24}$ | – | – | 245.2/270 [C/$\chi^2$] |
| | MCG−01 − 26 −013 | – | $0.36^{+0.31}_{-0.11}$ | $1.82^{+0.57}_{-0.71}$ | – | – | 44.9/53 [C/$\chi^2$] |
| F12043−3140 | ESO440−IG058N | – | – | $1.76^{+0.44}_{-0.46}$ | – | – | 40.1/45 [C] |
| | ESO440−IG058S | – | $0.97^{+0.21}_{-0.17}$ | $2.32^{+0.21}_{-0.17}$ | – | – | 66.7/71 [C] |
| F12590+2934 | NGC 4922N | $7.7^{+4.0}_{-2.8}$ | $0.62^{+0.27}_{-0.33}$ | 2.11[a] | $\geq$427 | $2.11^{+0.44}_{-0.46}$ | 56.3/108 [C/$\chi^2$] |
| F13197−1627 | MCG−03 − 34 − 064[b] | – | $0.85^{+0.04}_{-0.02}/1.67^{+0.17}_{-0.06}$ | 2.80[a] | $54.2^{+0.7}_{-0.9}$ | $2.80^{+0.18}_{-0.05}$ | 1805.1/1396 [$\chi^2$] |
| F14544−4255 | IC 4518A | – | $0.77^{+0.04}_{-0.05}$ | 1.72[a] | $24 \pm 2$ | $1.72^{+0.09}_{-0.05}$ | 399.2/331 [$\chi^2$] |
| | IC 4518B | $3.1^{+2.9}_{-2.5}$ | $0.24^{+0.20}_{-0.06}$ | 1.9[a] | $32^{+41}_{-14}$ | 1.9[c] | 165.7/188 [C] |
| F16577+5900 | NGC 6285 | – | – | $1.64 \pm 0.62$ | – | – | 16.8/16 [C] |
| F17138−1017 | IRASF17138−1017 | – | – | $1.13^{+0.17}_{-0.16}$ | – | – | 108.2/131 [C/$\chi^2$] |
| 20264+2533 | MCG +04−48 −002 | – | $0.76^{+0.23}_{-0.25}$ | 1.50[a] | $58^{+7}_{-4}$ | $1.50^{+0.12}_{-0.14}$ | 185.5/169 [$\chi^2$] |
| | NGC 6921 | – | $0.63^{+0.34}_{-0.52}$ | 2.08[a] | $178^{+30}_{-53}$ | $2.08^{+0.16}_{-0.39}$ | 64.7/82 [$\chi^2$] |
| F21453−3511 | NGC 7130 | $5.0 \pm 1.2$ | $0.24^{+0.07}_{-0.06}/0.79^{+0.25}_{-0.09}$ | 2.36[a] | $407^{+152}_{-91}$ | $2.36^{+0.20}_{-0.12}$ | 330.5/346 [C/$\chi^2$] |
| F23007+0836 | NGC 7469 | – | – | – | $0.006 \pm 0.002$ | $2.12^{+0.14}_{-0.09}$ | 1923.5/1766 [$\chi^2$] |
| 23262+0314 | NGC 7679 | – | $0.63^{+0.12}_{-0.10}$ | – | $\leq$0.02 | $1.66 \pm 0.04$ | 278.9/259 [$\chi^2$] |
| | NGC 7682 | – | $0.26^{+0.08}_{-0.05}$ | 2.27[a] | $243^{+60}_{-44}$ | $2.27^{+0.18}_{-0.17}$ | 876.2/914 [C] |

[a]Value of $\Gamma_{\rm bin.}$ fixed to that of the AGN continuum ($\Gamma$); [b]Additional plasma ($kT = 0.11^{+0.01}_{-0.06}$ keV); [c]Value fixed.

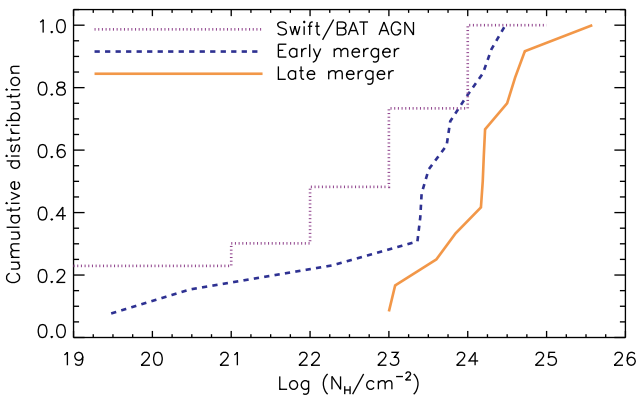


**Figure 9.** Cumulative $N_{\rm H}$ distribution for AGN in early- (blue dashed line) and late-merger (orange continuous line) galaxies. For comparison, we also show the cumulative intrinsic $N_{\rm H}$ distribution of local, mostly non-merging *Swift*/BAT AGN (purple dotted line) from Ricci et al. (2015). The plot shows that: (i) AGN in late mergers are systematically more obscured than those in early mergers and *Swift*/BAT AGN; (ii) all AGN in late mergers have $N_{\rm H} \geq 10^{23}$ cm$^{-2}$, which implies that they are almost completely surrounded by material with $N_{\rm H} \geq 10^{23}$ cm$^{-2}$. Following the approach described in Cameron (2011), we found that the obscuring material covers $95^{+4}_{-8}$ per cent of the X-ray source, where the uncertainties represent the 16th and 84th quantiles of a binomial distribution.

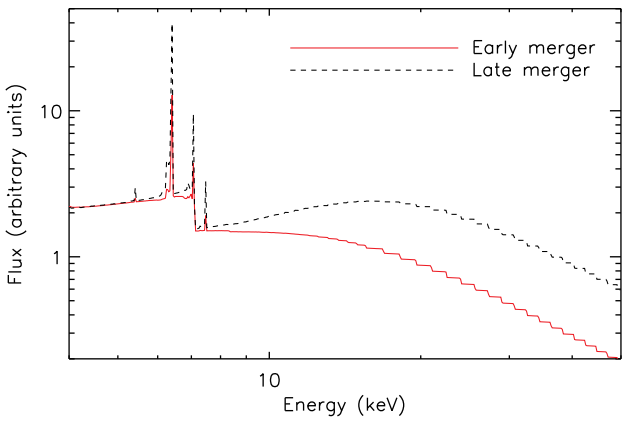


**Figure 10.** Average best-fitting spectral model for the AGN in galaxies in early (red continuous line) and late (black dashed line) merger stage. Each individual spectral model was normalized to have the same flux in the 4–50 keV range. The two average spectral models were then normalized to have the same flux in the 4–5 keV band for visualization purposes. The figure clearly illustrates the different mean spectra of the two subsamples, with AGN in late-merger galaxies showing more prominent features of heavy absorption (i.e. Fe K$\alpha$ line at 6.4 keV and Compton hump at ∼20–30 keV) than those in early-merger galaxies.

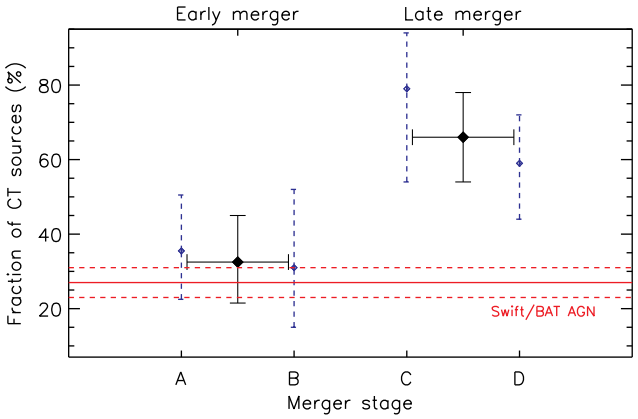


**Figure 11.** Fraction of CT (i.e. $N_{\rm H} \geq 10^{24}\,{\rm cm}^{-2}$) AGN versus merger stage. The empty blue diamonds represent the values for the four merger stages separately, while the filled black diamonds are the values for early and late mergers. The uncertainties represent the 16th/84th quantiles of a binomial distribution. The red continuous line represents the intrinsic fraction of CT AGN measured by *Swift*/BAT (Ricci et al. 2015) for local hard X-ray selected AGN, while the dashed lines are the $1\sigma$ uncertainty associated with this value. The figure shows that AGN in the late stages of mergers are more likely to be CT than those in isolated galaxies, which confirms the idea that the amount of dense material around the SMBH is larger in advanced mergers.

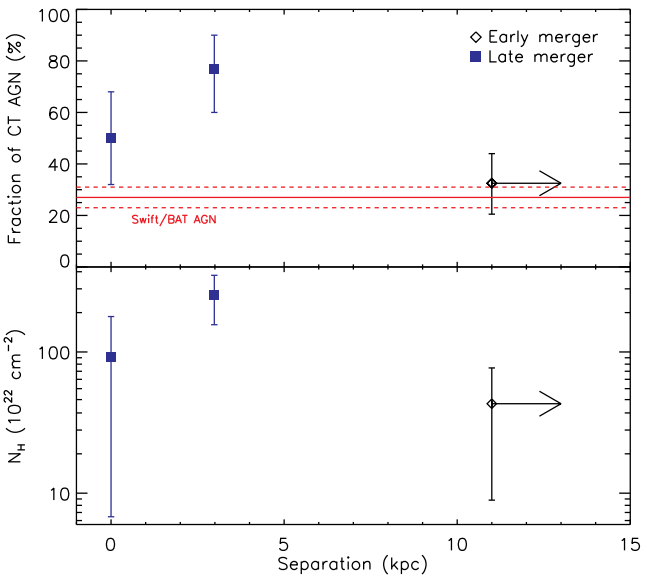


**Figure 12.** Top panel: fraction of CT AGN versus the separation between the two galactic nuclei. U/LIRGs in the late stages of galaxy mergers are divided into objects with two nuclei and those with a single nucleus. The separation for U/LIRGs in late-merger stages showing two nuclei is set to the mean value of the distance, while for objects with a single nucleus we set it to zero kpc. The red continuous line represents the intrinsic fraction of CT AGN measured by *Swift*/BAT (Ricci et al. 2015) for local hard X-ray selected AGN. The uncertainties on $f_{\rm CT}$ represent the 16th/84th quantiles of a binomial distribution. Bottom panel: median value of the line-of-sight column density versus the separation between the two galactic nuclei. The error bars on $N_{\rm H}$ show the $1\sigma$ interval. The three objects (NGC 4922N, Arp 220W and NGC 7674) for which only a lower limit of $N_{\rm H}$ could be constrained were assigned the minimum value. The two plots show that nuclear obscuration seems to peak when the two nuclei are at a distance of 0.4–10.8 kpc.

fraction of CT AGN in early-merger stage galaxies ($35^{+13}_{-12}$ per cent) is marginally lower than in late-merger stage galaxies, and is consistent with that of local hard X-ray selected AGN (Fig. 11). All the uncertainties reported on the fractions of AGN represent the 16th and 84th quantiles of a binomial distribution, computed with the beta function (Cameron 2011).

Dividing the sample based on the distance between the nuclei of the merging galaxies (top panel of Fig. 12), we find that the fraction of CT AGN peaks ($77^{+13}_{-17}$ per cent) when the sources are in late-merger stages and at a projected distance of 0.4–10.8 kpc. The median column density (bottom panel of Fig. 12) also reaches its maximum value at this stage [$N_{\rm H} = (2.53 \pm 0.97) \times 10^{24}\,{\rm cm}^{-2}$], and is larger than for early mergers at a distance $\geq$11 kpc [$N_{\rm H} = (4.3 \pm 3.4) \times 10^{23}\,{\rm cm}^{-2}$]. In agreement with these X-ray-based results, a further four nuclei (the NW and SE nuclei of IRAS 08572+3915, NGC 3690E and IRAS 14378−3651) in the sample have indications for the presence of accreting SMBHs from other multiwavelength tracers, although they are only weakly or not detected by *NuSTAR* (and are therefore very likely heavily obscured). All are in late stage of mergers, with three of them being in systems in which the two galactic nuclei are separated by a few kiloparsecs (see Appendix A).

The increase of the fraction of CT AGN along the merger sequence is in strong agreement with the long-standing paradigm that galaxy mergers are able to trigger the inflow of material on to the close environment of SMBHs. Recent numerical simulations of mergers (Blecha et al. in preparation) show that an increase in $N_{\rm H}$ caused by the merger dynamics is expected as the distance between the two nuclei decreases. Because these simulations can only probe column densities on resolved scales ($\gtrsim$48 pc), they provide a lower limit on the total line-of-sight obscuration. On scales of $\gtrsim$48 pc, the median value of $N_{\rm H}$ predicted by the simulations ($N_{\rm H} \simeq 3 \times 10^{23}\,{\rm cm}^{-2}$) is significantly lower than what we found here, and the simulations shows that AGN can be obscured by CT material only for a very brief phase around coalescence. This could imply that the material responsible for most of the obscuration is located on scales smaller than those probed by the simulations (i.e. $\lesssim$48 pc). Our findings are consistent with recent observations carried out in the submm band, which found evidence of Compact Obscuring Nuclei (CON; Aalto et al. 2015) in U/LIRGS (e.g. Sakamoto et al. 2010; Costagliola et al. 2013; Martín et al. 2016). These CON typically have sizes of tens of parsecs (e.g. Aalto et al. 2015; Scoville et al. 2015), and the high column densities ($N_{\rm H} > 10^{24}\,{\rm cm}^{-2}$) inferred from the submm observations may be responsible for the bulk of the obscuration traced by the X-rays.

According to the classical unification scheme of AGN (Antonucci 1993), obscuration is only due to anisotropic material distributed in the form of a torus, and the sole difference between obscured and unobscured objects is the inclination of the observer with respect to the torus. The fraction of CT AGN in mergers vastly exceeds that expected considering a random viewing angle with respect to the torus, and this enhanced obscuration is indicative of additional material on pc scales. Moreover, as illustrated in Fig. 9, AGN in late mergers are almost completely surrounded by material with $N_{\rm H} \geq 10^{23}\,{\rm cm}^{-2}$, which covers $95^{+4}_{-8}$ per cent of the solid angle of the accreting SMBH.[5] As a comparison, the covering

[5] The covering factor was calculated following the approach described in Cameron (2011), and the uncertainties represent the 16th and 84th quantiles of a binomial distribution.

factor of material with $\log(N_{\rm H}/{\rm cm}^{-2}) = 23-25$ in *Swift*/BAT AGN is $52 \pm 2$ per cent (Ricci et al. 2015). This implies that the classical unification scenario is not sufficient to describe the structure of obscuration in galaxies undergoing mergers. Our results can be interpreted in the framework of the AGN evolutionary model first proposed by Sanders et al. (1988) for U/LIRGS. This scenario starts with a merger of galaxies, which triggers accretion and heavy obscuration, along with strong starbursts, and is then followed by a phase in which feedback from the AGN removes the obscuring material and the source can be observed as a red quasar (e.g. Urrutia, Lacy & Becker 2008; Banerji et al. 2012; LaMassa et al. 2016). The object eventually ends its life as an unobscured quasar (e.g. Treister et al. 2010). Here, we find a hint of a decrease in the fraction of CT AGN and in the median $N_{\rm H}$ with the separation (for $D_{12} < 11$ kpc). In particular, closely separated nuclei seem to have a larger fraction of CT AGN than objects in the single-nuclei phase, which in the evolutionary scheme would be the stage when the AGN is starting to clean up its environment. This behaviour, if confirmed, would also be in agreement with recent numerical simulations (Blecha et al. in preparation).

Several studies over the past years have shown that the fraction of AGN in mergers increases with the AGN luminosity (e.g. Treister et al. 2012; Glikman et al. 2015), reaching ∼40–80 per cent at bolometric luminosities of $\log(L_{\rm Bol}/{\rm erg\,s}^{-1}) \sim 46-48$, in agreement with the idea that mergers of galaxies are able to effectively fuel SMBHs. This picture is consistent with what has been recently found for mid-IR selected Hot Dust-obscured galaxies (e.g. Eisenhardt et al. 2012; Wu et al. 2012; Assef et al. 2015), which host the most luminous obscured AGN known (e.g. Stern et al. 2014; Piconcelli et al. 2015; Assef et al. 2016; Ricci et al. 2017), show an excess of submillimetre galaxies as neighbours (Jones et al. 2015), and tend to be found in mergers of galaxies (Fan et al. 2016). Some recent studies of galaxies at $z \sim 0.6$–$0.7$ (e.g. Villforth et al. 2014, 2017) have argued that the fraction of AGN in mergers is significantly lower, and it does not increase with the AGN bolometric luminosity. However, the samples used for these studies were selected in the soft X-ray band, which is strongly biased against heavily obscured sources. In particular, Villforth et al. (2017) used a *ROSAT*-selected sample, which, in the rest frame of the sources they considered, corresponds to a selection in the ∼0.2–3.8 keV band. Our work shows that the circumnuclear environment of AGN in mergers is different (i.e. richer in gas and dust) from that of AGN in isolated galaxies, which implies that soft X-ray selection would fail to detect most of the AGN in mergers. Considering the median $N_{\rm H}$ of sources in advanced stages of merger with two distinct nuclei [$N_{\rm H} = (2.53 \pm 0.97) \times 10^{24}\,{\rm cm}^{-2}$], which would be the sources easier to distinguish as mergers at $z \sim 0.6$, the AGN would lose ∼99.9 per cent of the ∼0.2–3.8 keV flux.

Treister et al. (2012) showed that, while 90 per cent of AGN are triggered by secular processes (i.e. stellar bars, supernova winds, etc.), ∼50–60 per cent of the SMBH growth is caused by mergers. Since mergers are predicted to be ubiquitous and play a fundamental role in the formation and evolution of galaxies (Springel et al. 2005), accretion triggered by tidal torques could contribute significantly to the growth of SMBHs, and could produce the observed relation between the mass of the SMBH and the velocity dispersion of the galaxy bulge (e.g. Di Matteo et al. 2005; Blecha et al. 2011). With the *NuSTAR* observations analysed here, we show that mergers of galaxies are able to drive material into the proximity of the SMBH, thus strengthening the idea that interactions between galaxies are critical to understand the link between accreting SMBHs and their hosts.

## 6 SUMMARY AND CONCLUSIONS

In this work, we studied the relation between AGN obscuration and galaxy mergers. This was done analysing the broad-band X-ray emission of a sample of 30 U/LIRGs in different merger stages from the GOALS sample (for a total of 52 individual galactic nuclei). In a forthcoming paper (Ricci et al., in preparation), we will discuss the multiwavelength properties of the U/LIRGs of our sample, and how they relate to the bolometric luminosity of the AGN. In the following, we summarize our findings.

(i) All AGN of our sample in late-merger galaxies have $N_{\rm H} \geq 10^{23}\,{\rm cm}^{-2}$, which implies that the obscuring material covers $95^{+4}_{-8}$ per cent of the X-ray source (see Fig. 9). The close environment of these objects is therefore very different from what would be foreseen by the unification model of AGN.

(ii) The fraction of CT AGN in late-merger galaxies is higher ($f_{\rm CT} = 65^{+12}_{-13}$ per cent) than in local hard X-ray selected AGN ($f_{\rm CT} = 27 \pm 4$ per cent, Ricci et al. 2015), which are mostly found in isolated galaxies, and marginally higher than AGN in early-merger galaxies (see Figs 10 and 11).

(iii) A peak in the fraction of CT AGN is found when the nuclei of the two merging galaxies are at a projected distance of $\simeq$ 0.4–10.8 kiloparsecs ($f_{\rm CT} = 77^{+13}_{-17}$ per cent, see Fig. 12). This is also the stage at which the maximum of the median $N_{\rm H}$ is observed [$N_{\rm H} = (2.53 \pm 0.97) \times 10^{24}\,{\rm cm}^{-2}$]. We also find a hint of a decrease both in $f_{\rm CT}$ and in the median $N_{\rm H}$ when only a single nucleus is observed. If confirmed, this decrease of the obscuring material might be related to feedback from the AGN clearing out its environment.

Our results confirm the long-standing idea that galaxy mergers are able to trigger the inflow of material on to the inner tens of parsecs, and that the close environment of AGN in late-merger galaxies is richer in gas and dust as compared to AGN in isolated galaxies.

## ACKNOWLEDGEMENTS

We thank the referee for the careful reading of the manuscript and for the prompt report that helped us improve the quality of the paper. We thank the *NuSTAR* Cycle 1 TAC for the *NuSTAR* data on which this paper is based, Chin-Shin Chang, George Lansbury, Dave Alexander and Johannes Buchner for useful comments on the manuscript. This work made use of data from the *NuSTAR* mission, a project led by the California Institute of Technology, managed by the Jet Propulsion Laboratory and funded by the National Aeronautics and Space Administration. We thank the *NuSTAR* Operations, Software and Calibration teams for support with the execution and analysis of these observations. This research has made use of the *NuSTAR* Data Analysis Software (NUSTARDAS) jointly developed by the ASI Science Data Center (ASDC, Italy) and the California Institute of Technology (Caltech, USA), and of the NASA/ IPAC Infrared Science Archive and NASA/IPAC Extragalactic Database (NED), which are operated by the Jet Propulsion Laboratory, California Institute of Technology, under contract with the National Aeronautics and Space Administration. We acknowledge financial support from the CONICYT-Chile grants 'EMBIGGEN' Anillo ACT1101 (CR, FEB, ET), FONDECYT 1141218 (CR, FEB), FONDECYT 1160999 (ET), FONDECYT 3150361 (GP), Basal-CATA PFB–06/2007 (CR, FEB, ET), the NASA *NuSTAR* AO1 Award NNX15AV27G (FEB), the China-CONICYT fund (CR), the Swiss National Science Foundation (Grant PP00P2_138979/1 and PP00P2_166159, KS), the Chinese Academy of Science grant

No. XDB09030102 (LH), the National Natural Science Foundation of China grant No. 11473002 (LH), the Ministry of Science and Technology of China grant No. 2016YFA0400702 (LH), the Spanish MINECO (KI) under grant AYA2013-47447-C3-2-P and MDM-2014-0369 of ICCUB (Unidad de Excelencia 'María de Maeztu') and the Ministry of Economy, Development, and Tourism's Millennium Science Initiative through grant IC120009, awarded to The Millennium Institute of Astrophysics, MAS (FEB).

## REFERENCES

Aalto S. et al., 2015, A&A, 584, A42
Alonso-Herrero A., García-Marín M., Monreal-Ibero A., Colina L., Arribas S., Alfonso-Garzón J., Labiano A., 2009, A&A, 506, 1541
Alonso-Herrero A. et al., 2013, ApJ, 779, L14
Annuar A. et al., 2015, ApJ, 815, 36
Antonucci R., 1993, ARA&A, 31, 473
Armus L. et al., 2009, PASP, 121, 559
Arnaud K. A., 1996, in Jacoby G. H., Barnes J., eds, ASP Conf. Ser. Vol. 101, Astronomical Data Analysis Software and Systems V. Astron. Soc. Pac., San Francisco, p. 17
Assef R. J. et al., 2015, ApJ, 804, 27
Assef R. J. et al., 2016, ApJ, 819, 111
Ballo L., Braito V., Della Ceca R., Maraschi L., Tavecchio F., Dadina M., 2004, ApJ, 600, 634
Baloković M. et al., 2014, ApJ, 794, 111
Banerji M., McMahon R. G., Hewett P. C., Alaghband-Zadeh S., Gonzalez-Solares E., Venemans B. P., Hawthorn M. J., 2012, MNRAS, 427, 2275
Baumgartner W. H., Tueller J., Markwardt C. B., Skinner G. K., Barthelmy S., Mushotzky R. F., Evans P. A., Gehrels N., 2013, ApJS, 207, 19
Bessiere P. S., Tadhunter C. N., Ramos Almeida C., Villar Martín M., 2012, MNRAS, 426, 276
Blecha L., Cox T. J., Loeb A., Hernquist L., 2011, MNRAS, 412, 2154
Blustin A. J., Branduardi-Raymont G., Behar E. et al., 2003, A&A, 403, 481
Boorman P. G., Gandhi P., Alexander D. M. et al., 2016, ApJ, 833, 245
Brightman M., Nandra K., 2011, MNRAS, 413, 1206
Brightman M. et al., 2015, ApJ, 805, 41
Burlon D., Ajello M., Greiner J., Comastri A., Merloni A., Gehrels N., 2011, ApJ, 728, 58
Burrows D. N. et al., 2005, Space Sci. Rev., 120, 165
Cameron E., 2011, PASA, 28, 128
Cash W., 1979, ApJ, 228, 939
Chiaberge M., Gilli R., Lotz J. M., Norman C., 2015, ApJ, 806, 147
Costagliola F., Aalto S., Sakamoto K., Martín S. Beswick R., Muller S., Klöckner H.-R., 2013, A&A, 556, A66
Dadina M., 2007, A&A, 461, 1209
Davies R. L., Rich J. A., Kewley L. J., Dopita M. A., 2014, MNRAS, 439, 3835
Davies R. L. et al., 2016, MNRAS, 462, 1616
Del Moro A. et al., 2016, MNRAS, 456, 2105
Della Ceca R. et al., 2002, ApJ, 581, L9
Di Matteo T., Springel V., Hernquist L., 2005, Nature, 433, 604
Díaz-Santos T. et al., 2011, ApJ, 741, 32
Díaz-Santos T. et al., 2013, ApJ, 774, 68
Díaz-Santos T. et al., 2014, ApJ, 788, L17
Downes D., Eckart A., 2007, A&A, 468, L57
Duc P.-A., Mirabel I. F., Maza J., 1997, A&AS, 124
Dudik R. P., Satyapal S., Marcu D., 2009, ApJ, 691, 1501
Eisenhardt P. R. M. et al., 2012, ApJ, 755, 173
Ellison S. L., Patton D. R., Mendel J. T., Scudder J. M., 2011, MNRAS, 418, 2043
Evans A. S., Mazzarella J. M., Surace J. A., Sanders D. B., 2002, ApJ, 580, 749
Fan L. et al., 2016, ApJ, 822, L32
Ferrarese L., Merritt D., 2000, ApJ, 539, L9
Feruglio C., Maiolino R., Piconcelli E., Menci N., Aussel H., Lamastra A., Fiore F., 2010, A&A, 518, L155
Feruglio C. et al., 2015, A&A, 583, A99
Gabriel C. et al., 2004, in Ochsenbein F., Allen M. G., Egret D., eds, ASP Conf. Ser. Vol. 314, Astronomical Data Analysis Software and Systems (ADASS) XIII. Astron. Soc Pac., San Francisco, p. 759
Gandhi P. et al., 2014, ApJ, 792, 117
Gandhi P. et al., 2016, preprint (arXiv:e-prints)
Garmire G. P., Bautz M. W., Ford P. G., Nousek J. A., Ricker G. R., Jr, 2003, in Truemper J. E., Tananbaum H. D., eds, Proc. SPIE Conf. Ser. Vol. 4851, X-Ray and Gamma-Ray Telescopes and Instruments for Astronomy. SPIE, Bellingham, p. 28
Gebhardt K. et al., 2000, ApJ, 539, L13
Gilli R., Vignali C., Mignoli M., Iwasawa K., Comastri A., Zamorani G., 2010, A&A, 519, A92
Glikman E., Simmons B., Mailly M., Schawinski K., Urry C. M., Lacy M., 2015, ApJ, 806, 218
González-Martín O. et al., 2016, A&A, 587, A1
Griffith R. L. et al., 2011, ApJ, 736, L22
Haan S. et al., 2011, AJ, 141, 100
Hainline K. N., Reines A. E., Greene J. E., Stern D., 2016, ApJ, 832, 119
Harrison F. A. et al., 2013, ApJ, 770, 103
Hernán-Caballero A. et al., 2015, ApJ, 803, 109
Hernquist L., 1989, Nature, 340, 687
Hickox R. C., Mullaney J. R., Alexander D. M., Chen C.-T. J., Civano F. M., Goulding A. D., Hainline K. N., 2014, ApJ, 782, 9
Ho L. C., Filippenko A. V., Sargent W. L. W., 1997, ApJS, 112, 315
Hopkins P. F., Hernquist L., Cox T. J., Di Matteo T., Robertson B., Springel V., 2006, ApJS, 163, 1
Howell J. H. et al., 2010, ApJ, 715, 572
Huchra J., Burg R., 1992, ApJ, 393, 90
Ichikawa K., Imanishi M., Ueda Y., Nakagawa T., Shirahata M., Kaneda H., Oyabu S., 2014, ApJ, 794, 139
Imanishi M., Terashima Y., 2004, AJ, 127, 758
Imanishi M., Terashima Y., Anabuki N., Nakagawa T., 2003, ApJ, 596, L167
Imanishi M., Nakagawa T., Ohyama Y., Shirahata M., Wada T., Onaka T., Oi N., 2008, PASJ, 60, S489
Imanishi M., Nakagawa T., Shirahata M., Ohyama Y., Onaka T., 2010, ApJ, 721, 1233
Inami H. et al., 2010, AJ, 140, 63
Inami H. et al., 2013, ApJ, 777, 156
Iwasawa K., Comastri A., 1998, MNRAS, 297, 1219
Iwasawa K., Sanders D. B., Evans A. S., Trentham N., Miniutti G., Spoon H. W. W., 2005, MNRAS, 357, 565
Iwasawa K. et al., 2011a, A&A, 528, A137
Iwasawa K. et al., 2011b, A&A, 529, A106
Jansen F. et al., 2001, A&A, 365, L1
Jones S. F. et al., 2015, MNRAS, 448, 3325
Kalberla P. M. W., Burton W. B., Hartmann D., Arnal E. M., Bajaja E., Morras R., Pöppel W G L., 2005, A&A, 440, 775
Kartaltepe J. S. et al., 2010, ApJ, 709, 572
Kim D.-C., Sanders D. B., 1998, ApJS, 119, 41
Kocevski D. D. et al., 2015, ApJ, 814, 104
Komossa S., Burwitz V., Hasinger G., Predehl P., Kaastra J. S., Ikebe Y., 2003, ApJ, 582, L15
Kormendy J., Ho L. C., 2013, ARA&A, 51, 511
Koss M., Mushotzky R., Veilleux S., Winter L., 2010, ApJ, 716, L125
Koss M., Mushotzky R., Treister E., Veilleux S., Vasudevan R., Trippe M., 2012, ApJ, 746, L22
Koss M., Mushotzky R., Baumgartner W., Veilleux S., Tueller J., Markwardt C., Casey C. M., 2013, ApJ, 765, L26
Koss M. J. et al., 2016a, ApJ, 824, L4
Koss M. J. et al., 2016b, ApJ, 825, 85
LaMassa S. M. et al., 2016, ApJ, 820, 70
Lansbury G. B. et al., 2014, ApJ, 785, 17
Lansbury G. B. et al., 2015, ApJ, 809, 115
Lanzuisi G. et al., 2015, A&A, 573, A137
Lehmer B. D. et al., 2015, ApJ, 806, 126
Levenson N. A., Weaver K. A., Heckman T. M., Awaki H., Terashima Y., 2005, ApJ, 618, 167

Lípari S., Díaz R., Taniguchi Y., Terlevich R., Dottori H., Carranza G., 2000, AJ, 120, 645
Lira P., Ward M., Zezas A., Alonso-Herrero A., Ueno S., 2002a, MNRAS, 330, 259
Lira P., Ward M. J., Zezas A., Murray S. S., 2002b, MNRAS, 333, 709
Madsen K. K., Harrison F. A., Markwardt C. B. et al., 2015, ApJS, 220, 8
Magdziarz P., Zdziarski A. A., 1995, MNRAS, 273, 837
Martín S. et al., 2016, A&A, 590, A25
Masetti N. et al., 2006, A&A, 455, 11
Masetti N. et al., 2008, A&A, 482, 113
Matt G., Perola G. C., Piro L., 1991, A&A, 247, 25
Miniutti G., Ponti G., Dadina M., Cappi M., Malaguti G., 2007, MNRAS, 375, 227
Murphy K. D., Yaqoob T., 2009, MNRAS, 397, 1549
Nardini E., Risaliti G., Watabe Y., Salvati M., Sani E., 2010, MNRAS, 405, 2505
Norris R. P., Forbes D. A., 1995, ApJ, 446, 594
O'Sullivan E. et al., 2014, ApJ, 793, 74
Oda S., Tanimoto A., Ueda Y., Imanishi M., Terashima Y., Ricci C., 2017, ApJ, 835, 179
Pereira-Santaella M., Diamond-Stanic A. M., Alonso-Herrero A., Rieke G. H., 2010, ApJ, 725, 2270
Petric A. O. et al., 2011, ApJ, 730, 28
Piconcelli E. et al., 2015, A&A, 574, L9
Privon G. C. et al., 2015, ApJ, 814, 39
Privon G. C. et al., 2017, ApJ, 835, 213
Ptak A., Heckman T., Levenson N. A., Weaver K., Strickland D., 2003, ApJ, 592, 782
Ptak A. et al., 2015, ApJ, 800, 104
Puccetti S. et al., 2016, A&A, 585, A157
Ramos Almeida C., Tadhunter C. N., Inskip K. J., Morganti R., Holt J., Dicken D., 2011, MNRAS, 410, 1550
Ranalli P., Comastri A., Setti G., 2003, A&A, 399, 39
Ricci C., Ueda Y., Paltani S., Ichikawa K., Gandhi P., Awaki H., 2014, MNRAS, 441, 3622
Ricci C., Ueda Y., Koss M. J., Trakhtenbrot B., Bauer F. E., Gandhi P., 2015, ApJ, 815, L13
Ricci C. et al., 2016a, ApJ, 819, 4
Ricci C. et al., 2016b, ApJ, 820, 5
Ricci C. et al., 2017, ApJ, 835, 105
Risaliti G., 2002, A&A, 386, 379
Risaliti G. et al., 2006, MNRAS, 365, 303
Romero-Cañizales C. et al., 2012, A&A, 543, A72
Rupke D. S. N., Veilleux S., 2013, ApJ, 768, 75
Sakamoto K., Aalto S., Evans A. S., Wiedner M. C., Wilner D. J., 2010, ApJ, 725, L228
Sanders D. B., Soifer B. T., Elias J. H., Madore B. F., Matthews K., Neugebauer G., Scoville N. Z., 1988, ApJ, 325, 74
Sanders D. B., Mazzarella J. M., Kim D.-C., Surace J. A., Soifer B. T., 2003, AJ, 126, 1607
Sani E. et al., 2008, ApJ, 675, 96
Satyapal S., Ellison S. L., McAlpine W., Hickox R. C., Patton D. R., Mendel J. T., 2014, MNRAS, 441, 1297
Schawinski K., Simmons B. D., Urry C. M., Treister E., Glikman E., 2012, MNRAS, 425, L61
Scott J. E. et al., 2005, ApJ, 634, 193
Scoville N. Z. et al., 2000, AJ, 119, 991
Scoville N. et al., 2015, ApJ, 800, 70
Shlosman I., Begelman M. C., Frank J., 1990, Nature, 345, 679
Shu X. W., Yaqoob T., Wang J. X., 2010, ApJS, 187, 581
Silverman J. D. et al., 2011, ApJ, 743, 2
Singh V., Shastri P., Risaliti G., 2011, A&A, 532, A84
Springel V. et al., 2005, Nature, 435, 629
Stern D. et al., 2012, ApJ, 753, 30
Stern D. et al., 2014, ApJ, 794, 102
Stierwalt S. et al., 2013, ApJS, 206, 1
Stierwalt S. et al., 2014, ApJ, 790, 124
Strüder L. et al., 2001, A&A, 365, L18
Sturm E., Lutz D., Verma A., Netzer H., Sternberg A., Moorwood A. F. M., Oliva E., Genzel R., 2002, A&A, 393, 821
Teng S. H., Veilleux S., 2010, ApJ, 725, 1848
Teng S. H. et al., 2009, ApJ, 691, 261
Teng S. H. et al., 2014, ApJ, 785, 19
Teng S. H. et al., 2015, ApJ, 814, 56
Treister E., Natarajan P., Sanders D. B., Urry C. M., Schawinski K., Kartaltepe J., 2010, Science, 328, 600
Treister E., Schawinski K., Urry C. M., Simmons B. D., 2012, ApJ, 758, L39
Turner M. J. L. et al., 2001, A&A, 365, L27
Ueda Y. et al., 2007, ApJ, 664, L79
Urrutia T., Lacy M., Becker R. H., 2008, ApJ, 674, 80
Vardoulaki E. et al., 2015, A&A, 574, A4
Vasudevan R. V., Fabian A. C., 2007, MNRAS, 381, 1235
Vega O., Clemens M. S., Bressan A., Granato G. L., Silva L., Panuzzo P., 2008, A&A, 484, 631
Veilleux S., Kim D.-C., Sanders D. B., 1999, ApJ, 522, 113
Veilleux S. et al., 2009, ApJS, 182, 628
Véron-Cetty M.-P., Véron P., 2010, A&A, 518, A10
Vignati P. et al., 1999, A&A, 349, L57
Villforth C. et al., 2014, MNRAS, 439, 3342
Villforth C. et al., 2017, MNRAS, 466, 812
Walton D. J., Nardini E., Fabian A. C., Gallo L. C., Reis R. C., 2013, MNRAS, 428, 2901
Weedman D. W. et al., 2005, ApJ, 633, 706
Weisskopf M. C., Tananbaum H. D., Van Speybroeck L. P., O'Dell S. L., 2000, in Truemper J. E., Aschenbach B., eds, Proc. SPIE Conf. Ser. Vol. 4012, X-Ray Optics, Instruments, and Missions III. SPIE, Bellingham, p. 2
Wilms J., Allen A., McCray R., 2000, ApJ, 542, 914
Wright E. L. et al., 2010, AJ, 140, 1868
Wu J. et al., 2012, ApJ, 756, 96
Yamada R., Oyabu S., Kaneda H., Yamagishi M., Ishihara D., Kim J. H., Im M., 2013, PASJ, 65, 103
Yuan T.-T., Kewley L. J., Sanders D. B., 2010, ApJ, 709, 884

## APPENDIX A: NOTES ON INDIVIDUAL SOURCES

In the following, we report the details on the individual sources, including previous literature studies on the presence of an accreting SMBH using multiwavelength tracers of AGN activity. The proxies of AGN activity we use are the following:

(i) The presence of high-excitation mid-IR (MIR; 5–40 μm) emission lines (e.g. Sturm et al. 2002), and in particular [Ne v] 14.32 μm and [Ne v] 24.32 μm, indicate the presence of an AGN, since the ionization potential of [Ne v] is 97 eV, which is considered too high to be produced by star formation (e.g. Weedman et al. 2005).

(ii) The slope of the near-IR continuum, with a very red continuum ($\Gamma > 1$, with $F_\nu \propto \lambda^\Gamma$, Imanishi et al. 2010) suggesting the presence of a buried AGN (Risaliti et al. 2006; Imanishi et al. 2008; Sani et al. 2008). Similarly, we also used the *Wide-field Infrared Survey Explorer* satellite (*WISE*, Wright et al. 2010) colours, adopting $W1 - W2 > 0.8$ as threshold for the presence of an AGN (Stern et al. 2012). It should be however remarked that this tracer can be problematic for low-luminosity AGN in strongly star-forming galaxies (e.g. Griffith et al. 2011; Hainline et al. 2016).

(iii) The equivalent width (EW) of the 3.3 and 6.2 μm polycyclic aromatic hydrocarbon (PAH) features. PAH features are destroyed by the radiation field of the AGN or diluted by the strong MIR continuum, thus low values of the EW typically indicate the presence

of an AGN [EW(3.3 μm) < 40 nm, Imanishi et al. 2010; Ichikawa et al. 2014; EW(6.2 μm) < 0.27 μm, Stierwalt et al. 2013.

(iv) Optical line ratios. The U/LIRGs of our sample are optically classified as objects dominated by star formation in the optical band (i.e. H II regions; e.g. Ho, Filippenko & Sargent 1997), objects that might contain both star formation and AGN activity (i.e. composite objects; e.g. Yuan, Kewley & Sanders 2010), and objects that are clearly dominated by AGN activity (i.e. Seyfert 1s or Seyfert 2s).

(v) The spatial variations of the radio spectral index (i.e. radio-spectral-index maps; Vardoulaki et al. 2015) allow objects to be classified as radio AGN, composite AGN/starburst (SB) and radio starburst (radio-SB).

### A1 IRAS F00085−1223 (NGC 34)

The LIRG NGC 34 is in merger stage D, and shows a single nucleus (Fig. 4). The object is reported to be a Seyfert 2 by Yuan et al. (2010). Using the radio spectral index maps, Vardoulaki et al. (2015) also confirmed the presence of an AGN.

The source is detected by *NuSTAR* in the 3–10 keV (10–24 keV) band at 5.7$\sigma$ (6.3$\sigma$) and 6.8$\sigma$ (4.4$\sigma$) for FPMA and FPMB, respectively. The source is also detected by *Chandra* and by *XMM–Newton*. The X-ray spectrum of NGC 34 (Fig. B1) shows a clear Fe K$\alpha$ feature at $6.48^{+0.06}_{-0.05}$ keV, which also indicates the presence of an AGN. We therefore applied a model including both thermal emission and an AGN component (ATABLE{TORUS1006.FITS} + APEC + ZPOWERLAW). We added a cross-calibration constant between the different, non-simultaneous, observations. We found that the flux varied by a factor ∼2 between the *NuSTAR*, *Chandra* and *XMM–Newton* observations. Our spectral analysis shows that the AGN is heavily obscured, with a column density of $N_{\rm H} = 5.3 \pm 1.1 \times 10^{23}\,{\rm cm}^{-2}$. The value of the half-opening angle could not be constrained for this observation, and was therefore fixed to $\theta_{\rm OA} = 60$ deg. The scattered radiation has a flux of $6.2^{+7.9}_{-4.3}$ per cent of the primary X-ray emission in the X-ray energy band probed here.

### A2 IRAS F00163−1039 (Arp 256 and MCG−02 − 01 −052)

The two objects are in stage B, and their projected separation is 33.1 kpc (Fig. 4). While Arp 256 is a LIRG, the IR luminosity of MCG−02 − 01 −052 is $\log(L_{\rm IR}/{\rm L}_\odot) = 10.36$. Optically, Arp 256 is classified by Yuan et al. (2010) as an H II region, and none of the tracers detect an AGN in Arp 256 or MCG−02 − 01 −052.

The two galactic nuclei are at a distance (56.1 arcsec) that allows them to be well separated by *Chandra*. While the two galaxies are detected by *Chandra*, they are not detected by *NuSTAR*, with both nuclei only exhibiting significances of ∼3$\sigma$ in the 3–10 keV band and of <2$\sigma$ in the 10–24 keV band. The *Chandra* spectra of both sources are soft, and can be well fit by a starburst model. For Arp 256, a thermal plasma and a power-law component, both of which appear obscured [ZPHABS × (ZPOWERLAW+APEC)], are necessary to best reproduce the spectrum. The same model, with the exception of the absorbing component, was used for MCG−02 − 01 −052. The spectra and the fit are shown in Fig. B1.

### A3 IRAS F00506+7248 (MCG+12−02 −001)

This LIRG is in merger stage C, and the projected separation of the two nuclei is 0.3 kpc (Fig. 4). The system is classified in the optical as a composite (Alonso-Herrero et al. 2009), and none of the tracers analysed suggest the presence of an AGN.

While the system is detected by *Chandra*, it is not detected by *NuSTAR*, and the significance is <3$\sigma$ for each camera in the 3–10 keV and 10–24 keV band. Given the very small separation between the two nuclei (0.9 arcsec), the X-ray emission observed by *Chandra* could come from any of the two nuclei, or from both of them. The *Chandra* spectrum was fitted with a simple absorbed power-law model (ZPHABS×PO). Using the relation of Ranalli, Comastri & Setti (2003), we find that the star formation rate obtained for the source (∼54.5 $\rm M_\odot\,yr^{-1}$, Howell et al. 2010) is able to account for the totality of the 2–10 keV luminosity observed. The steep photon index obtained ($\Gamma \sim 3$) also suggests that the X-ray emission is related to star formation. The spectrum of the source is illustrated in Fig. B1.

### A4 IRAS F02069−1022 (NGC 833 and NGC 835)

IRAS F02069−1022 (also called Arp 318) is composed of two galaxies at a projected distance of 15.7 kpc and is in merger stage A (Fig. 4). The multiwavelength tracers fail to detect evidence of AGN activity, with the exception of optical spectroscopy for NGC 835, which is classified as a Seyfert 2 (Véron-Cetty & Véron 2010). NGC 835 hosts a low-luminosity AGN which appears responsible for most of the 2–10 keV emission (González-Martín et al. 2016). NGC 833 is classified as a low-ionization nuclear emission-line region (LINER; Véron-Cetty & Véron 2010), but it has been found to be AGN dominated, with a very low star formation rate ($\lesssim$3 $\rm M_\odot\,yr^{-1}$) over the past few hundreds of Myr (O'Sullivan et al. 2014).

The two galaxies are separated by 55.9 arcsec, and could be therefore well resolved by the *NuSTAR*, *XMM–Newton*/EPIC and *Chandra* observations studied by Oda et al. (in preparation), who found that both sources are strongly detected by *NuSTAR*. Oda et al. (in preparation) found that the analysis of the combined *XMM–Newton* EPIC, *Chandra*/ACIS and *NuSTAR* spectra of NGC 833 results in a column density of $N_{\rm H} = 2.8 \pm 0.3 \times 10^{23}\,{\rm cm}^{-2}$. Variability of the line-of-sight column density between the *Chandra* and *XMM–Newton* observations of NGC 835 was found by González-Martín et al. (2016). Oda et al. (in preparation) find that the *NuSTAR* spectrum is very different from the *XMM–Newton* observation carried out in 2000 January, while it is consistent with the spectrum of the more recent (2013 July) *Chandra* observation. Fitting separately the combined *Chandra*/*NuSTAR* spectra and the *XMM–Newton* spectrum, Oda et al. (in preparation) found that the column density varies from $N^a_{\rm H} = 5.5^{+1.5}_{-1.0} \times 10^{23}\,{\rm cm}^{-2}$ (*XMM–Newton*) to $N^b_{\rm H} = 3.0 \pm 0.2 \times 10^{23}\,{\rm cm}^{-2}$ (*Chandra*/*NuSTAR*). Through the rest of the paper, we use the mean value of the column density for this source ($N^{\rm mean}_{\rm H} = 4.3^{+1.5}_{-1.0} \times 10^{23}\,{\rm cm}^{-2}$).

### A5 IRAS F05054+1718 (CGCG 468−002E and CGCG 468−002W)

This system in merger stage B is composed of an eastern (CGCG 468−002E) and a western (CGCG 468−002W) component (Fig. 4). While the eastern object is a LIRG, the western component has a luminosity in the IR of $\log(L_{\rm IR}/{\rm L}_\odot) = 10.74$. The western component shows a [Ne V] line at 14.32 μm (Inami et al. 2013), which indicates the presence of an AGN. From the ratio of the [Ne V]/[Ne II] and [O IV]/[Ne II] lines the AGN is found to contribute to ∼25–30 per cent of the MIR emission (Petric et al. 2011). The western component also shows a weak (EW = 0.12μm) PAH 6.2 μm feature, indicative of a significant AGN

contribution to the MIR flux. None of the proxies of AGN activity find evidence of an AGN in the eastern component.

The two galaxies are separated by 29.6 arcsec, and could therefore be distinguished both by the *Swift*/XRT and the *NuSTAR* observations studied here. CGCG 468−002W is clearly detected by *NuSTAR* in both detectors (∼51$\sigma$ in 0.3–10 kev and ∼31$\sigma$ in 10–24 keV for both FPMA and FPMB). The source is also detected by *Swift*/XRT in the 0.3–10 keV band. The *Swift*/XRT spectrum of this source is comprised from the integration of several observations carried out within a month in late 2014. The model we used to fit the spectra is similar to that used for NGC 34, with the exception of the thermal plasma, which is not required by the data. We also added a line at 6.47 ± 0.07 keV (EW $= 211^{+61}_{-66}$ eV) to account for the observed excess at ∼6.4 keV. The model we used is ATABLE{TORUS1006.FITS} + ZGAUSS + ZPOWERLAW, and shows that the level of obscuration of the source is low [$N_{\rm H} = (1.50 \pm 0.09) \times 10^{22}$ cm$^{-2}$]. A cross-calibration constant was also added, and showed that the flux of *NuSTAR* is ∼1.5 times higher than that of the XRT observation. The ratio between the scattered power-law and the primary X-ray emission is 1.5 ± 0.5 per cent. The broad-band spectrum is illustrated in Fig. B1. CGCG 468−002E was detected by neither *Swift*/XRT (2–8 keV) nor by *NuSTAR* (10–24 keV).

### A6 IRAS 05189−2524

This merger stage D ULIRG shows a single nucleus (Fig. 4), which has been found to host an AGN using several proxies. The source shows strong 14.32 (Inami et al. 2013) and 24.32 μm (Pereira-Santaella et al. 2010) [Ne V] lines, and very weak PAH features at 3.3 μm (EW =10 nm, Imanishi et al. 2008) and at 6.2 μm (EW =0.03 μm, Stierwalt et al. 2013). Optically the source is classified as a Seyfert 2 (Yuan et al. 2010). The [Ne V]/[Ne II] and [O IV]/[Ne II] ratios indicate that the AGN contributes ∼50 per cent of the MIR flux.

Previous studies in the X-ray band have also confirmed the presence of an AGN. The source has been detected by *XMM–Newton* (Imanishi & Terashima 2004; Teng & Veilleux 2010), by *Chandra* (Ptak et al. 2003), and by the XIS camera on board *Suzaku* (Teng et al. 2009). These X-ray spectral studies have shown that the AGN is obscured, with a line-of-sight column density ∼$10^{23}$ cm$^{-2}$. The source has also been detected by *Swift*/BAT (Koss et al. 2013). IRAS 05189−2524 was detected by *NuSTAR* in three observations carried out in 2013 for a total of ∼54 ks (Teng et al. 2015). Analysing the combined *XMM–Newton* and *NuSTAR* spectrum, Teng et al. (2015) showed that the obscuration can be explained by considering two absorbers, with column densities of 5.2 ± 0.2 and $9.3^{+1.0}_{-0.7} \times 10^{22}$ cm$^{-2}$, covering ≃ 98 per cent and ≃ 74 per cent of the X-ray source, respectively. To account for the partial covering, for this object we considered $N_{\rm H}$ to be the sum of the two column densities weighted by the covering factor.

### A7 IRAS 08572+3915

IRAS 08572+3915 is a ULIRG in a merger stage D showing two distinct nuclei [north-west (NW) and south-east (SE)], located at a distance of 5.6 kpc (Fig. 5). While no [Ne V] emission line is detected (Pereira-Santaella et al. 2010; Inami et al. 2013), the system shows a very strong silicate absorption feature at 9.7 μm ($\tau \sim -3.58$) and weak PAH features at 3.3 μm (EW <5 nm, Imanishi et al. 2008) and at 6.2 μm (EW <0.03 μm, Stierwalt et al. 2013). Using the radio spectral index, Vardoulaki et al. (2015) also found results consistent with the presence of an AGN. Both the NW and the SE nuclei are classified as Seyfert 2s by Yuan et al. (2010).

The *NuSTAR* observation of this object did not yield significant detections of either unresolved nuclei (Teng et al. 2015). The source was also not detected by a previous *Suzaku* observation (Teng et al. 2009). Teng et al. (2015) argued that the source could be X-ray weak, although it cannot be excluded that it is heavily obscured, similar to what we find here for most of the sources showing two nuclei with a separation of a few kpc. Using CO, Evans et al. (2002) estimated the average column density to be in the range of $N_{\rm H} \sim$ (3–10) × $10^{24}$ for this system. The NW nucleus was detected by *Chandra*, and Teng et al. (2009) reported an observed 0.5–10 keV luminosity of ∼$2 \times 10^{41}$ erg s$^{-1}$. The hardness ratios points to a photon index of $\Gamma \sim -0.43$, also indicative of heavy obscuration. We conclude therefore that both nuclei are likely to host heavily obscured AGN, but do not use these sources since an estimation of $N_{\rm H}$ is lacking.

### A8 IRAS F09320+6134 (UGC 5101)

UGC 5101 is a ULIRG with a single nucleus, classified as merger stage D (Fig. 5). Multiwavelength studies have shown strong evidence for the presence of an AGN, such as 14.32 and 24.32 μm [Ne V] emission lines (Pereira-Santaella et al. 2010; Inami et al. 2013), and weak 3.3 μm (EW =33 nm, Imanishi et al. 2008) and 6.2 μm (EW=0.13 μm, Stierwalt et al. 2013) PAH features. The *WISE* $W1 - W2$ colour of UGC 5101 is 1.697 ($W2 = 8.34$ mag), consistent with a significant AGN MIR emission (Stern et al. 2012). In the optical, the source is reported as being a Seyfert 2 (Yuan et al. 2010).

*Chandra* and *XMM–Newton* observations of this object were studied by Imanishi et al. (2003), who found that the AGN is CT. UGC 5101 was also reported as CT by Ricci et al. (2015) analysing *XMM–Newton* and *Swift*/BAT data. This in agreement with the depth of the 9.7 μm silicate feature ($\tau_{9.7\mu\rm m} = -0.78$, Stierwalt et al. 2013), which could also suggest the presence of a buried AGN. A recent study carried out by Oda et al. (2017), who studied in detail the observations of this object carried out by *Chandra*, *XMM–Newton*, *Suzaku* and *NuSTAR*, confirmed the CT obscuration of the source ($N_{\rm H} = 1.32^{+0.32}_{-0.37} \times 10^{24}$ cm$^{-2}$).

### A9 IRAS F09333+4841 (MCG+08−18 −013 and MCG+08−18 −012)

These two merger stage A galaxies have a projected separation of 35.4 kpc (Fig. 5). While MCG+08−18 −013 is classified as a LIRG, the IR luminosity of MCG+08−18 −012 is $\log(L_{\rm IR}/L_{\odot}) = 9.93$. MCG+08−18 −013 is classified as a composite galaxy by Yuan et al. (2010), and none of the multiwavelength tracers identify an AGN in the system.

The two galaxies are separated by 66.5 arcsec, and could therefore be clearly resolved by both *Chandra* and *NuSTAR*. In each of the 0.3–2 and 3–8 keV *Chandra* images, only MCG+08−18 −013 is detected, showing extended emission in both bands. Neither nucleus is detected by *NuSTAR* in the 3–10 keV or 3–24 keV band. The X-ray spectral analysis was carried out using the *Chandra* data alone. The X-ray spectrum of MCG+08−18 −013 was fitted with an obscured power-law (ZPHABS × ZPOWERLAW) model. We found that the level of obscuration is low ($N_{\rm H} \sim 3 \times 10^{21}$ cm$^{-2}$) and the X-ray continuum is rather steep ($\Gamma \sim 2.3$). No additional thermal component is necessary, and the X-ray spectrum is fully consistent with a scenario in which star formation is the only mechanism

producing X-ray emission. The X-ray spectrum of MCG+08−18 −013 is shown in Fig. B1.

### A10 IRAS F10015−0614 (NGC 3110 and MCG−01 − 26 −013)

This system includes two galaxies in a merger stage A, with a projected separation of 37.7 kpc (Fig. 5). Of the two galaxies, only NGC 3110 is a LIRG. NGC 3110 is classified as a H II region by Yuan et al. (2010), and no trace of an AGN is evident for NGC 3110 and MCG−01 − 26 −013 from any of the multiwavelength properties.

The two galaxies are separated by 108.9 arcsec, and could therefore be clearly resolved by both *Chandra* and *NuSTAR*. Neither nucleus is detected by *NuSTAR* in the 3–10 keV or 10–24 keV band. The combined *Chandra*/ACIS and *XMM–Newton*/EPIC X-ray spectrum of NGC 3110 could be well fit by an absorbed collisionally ionized plasma plus a power law [ZPHABS × (ZPOWERLAW+APEC)]. We applied a similar model to MCG−01 − 26 −013, although this object did not require the presence of absorbing material along the line of sight (ZPOWERLAW+APEC). For both sources, the X-ray spectral analysis does not require the presence of an AGN. The X-ray spectra of these two sources are illustrated in Fig. B2.

### A11 IRAS F10257−4339 (NGC 3256)

NGC 3256 is a LIRG in stage D (Fig. 5), with two nuclei detected in the radio (Norris & Forbes 1995) with a projected separation of 1 kpc. None of the multiwavelength proxies of AGN activity indicate the presence of an accreting SMBH, and the optical spectrum has been classified as that of an H II region (Lípari et al. 2000).

The *Chandra* spectrum was studied by Lira et al. (2002a) who could detect both nuclei (separated by 5.1 arcsec), and found X-ray emission consistent with being purely from star formation. The spectrum is in fact very soft, and could be modelled by the superposition of three thermal plasma components or by a steep power law with a photon index $\Gamma \sim 3$. NGC 3256 was observed by *NuSTAR*, and the results were reported in Lehmer et al. (2015), who concluded that the emission at >3 keV detected by *NuSTAR* is produced by a population of 5–10 ultraluminous X-ray sources.

### A12 IRAS 10565+2448

IRAS 10565+2448 is a ULIRG in stage D (Fig. 5) showing two nuclei (east and west components) with a projected separation of 6.7 kpc (Scoville et al. 2000). The west component was classified as a composite galaxy in the optical by Yuan et al. (2010), and no evidence of AGN activity has been found from the multiwavelength properties of the object.

The two nuclei are separated by 7.4 arcsec, and *Chandra* observations could be able to resolve both of them. The source was detected in the X-rays by *Chandra* and *XMM–Newton* (Teng & Veilleux 2010; Iwasawa et al. 2011b), and the spectra were found to be consistent with a star formation origin of the X-ray emission. The galaxy was not detected in a 25 ks *NuSTAR* observation (Teng et al. 2015).

### A13 IRAS F11257+5850 (Arp 299)

Arp 299 is a LIRG in merger stage C, with two nuclei (NGC 3690W and NGC 3690E) at a projected separation of 4.6 kpc (Fig. 6). The eastern nucleus is often confused with IC 0694, which is a lenticular galaxy nearby. Both nuclei show signatures of AGN activity in different energy bands. NGC 3690W has a weak 3.3 μm PAH feature (EW =16 nm; Imanishi et al. 2010) and a red 2.5–5 μm continuum ($\Gamma_{2.5-5\,\mu m} = 1.9$; Imanishi et al. 2010). A red near-IR continuum is also found for NGC 3690E ($\Gamma_{2.5-5\,\mu m} = 1.05$; Imanishi et al. 2010). The *WISE* $W1 - W2$ colours of both nuclei are also consistent with AGN activity, being $W1 - W2 \sim 1.5$ ($W2 = 6.26$ mag) and $W1 - W2 \sim 1.0$ ($W2 = 8.28$ mag) for NGC 3690W and NGC 3690E, respectively. In the MIR the 6.2μm PAH feature is rather weak for both NGC 3690W (EW = 0.12 μm; Stierwalt et al. 2013) and NGC 3690E (EW = 0.38 μm; Stierwalt et al. 2013), and indicates AGN contributions to the MIR luminosities of each nucleus of ∼75 per cent and ∼20 per cent (Stierwalt et al. 2013), respectively. In the optical Yuan et al. (2010) classified NGC 3690W as a Seyfert 2 and NGC 3690E as a H II region.

The two nuclei are separated by 21.3 arcsec, and could be resolved in the X-ray band by several studies carried out in the past decade. The presence of a buried AGN in NGC 3690W was first found by Della Ceca et al. (2002) using *BeppoSAX* data. Combining *BeppoSAX* with *Chandra* and *XMM–Newton* observations, Ballo et al. (2004) confirmed the heavily obscured nature of the western component, detecting a prominent Fe K$\alpha$ line. Ballo et al. (2004) also argued for the presence of a CT AGN in NGC 3690E, which shows a strong Fe XXV line at 6.7 keV. Alonso-Herrero et al. (2013) using the CanariCam instrument on the 10.4-m Gran Telescopio Canarias found evidence of AGN activity in both nuclei. For NGC 3690E, they estimated that the AGN is ∼5 times less luminous than NGC 3690W and the material surrounding the SMBH has an extinction of $A_V \sim 24$ mag. More recently, studying the simultaneous *NuSTAR* and *Chandra* spectra of NGC 3690W in the 3–40 keV range, Ptak et al. (2015) found a column density of $N_H \sim 4 \times 10^{24}$ cm$^{-2}$. No evidence of X-ray emission above 10 keV from NGC 3690E was found, and Ptak et al. (2015) concluded that the AGN is heavily obscured and/or significantly less luminous than NGC 3690W. Both NGC 3690W and NGC 3690E show deep silicate features ($\tau_{9.7\,\mu m} = -0.77$ and $-1.65$, respectively; Stierwalt et al. 2013), consistent with a buried AGN scenario.

### A14 IRAS F12043−3140 (ESO 440−IG058N and ESO 440−IG058S)

The two objects are in merger stage B, and their projected separation is 5.9 kpc (Fig. 6). The northern source is a LIRG, while the southern source has an IR luminosity of $\log(L_{IR}/L_\odot) = 10.54$. In the optical, ESO 440−IG058N has been classified as an H II region, while ESO 440−IG058S as a composite system (Yuan et al. 2010). Both galaxies show strong 6.2 μm PAH features (EW =0.56 and 0.66 μm for ESO 440−IG058N and ESO 440−IG058S, respectively; Stierwalt et al. 2013), and none of the tracers considered demonstrate the presence of an AGN.

The two sources are at 12 arcsec, and both have been detected by *Chandra*. No source was detected by *NuSTAR* at the position of the system, and therefore the spectral analysis was carried out using only *Chandra*. The X-ray spectrum of ESO 440−IG058N was fitted using a simple power-law model, with no absorption required (ZPOWERLAW). The model used for ESO 440−IG058S takes into account thermal emission and a power-law component (ZPOWERLAW+APEC). Both sources are consistent with no AGN contribution in the X-ray band, and their X-ray spectra are shown in Fig. B2.

### A15 IRAS F12540+5708 (Mrk 231)

Mrk 231 is an ULIRG with a single nucleus in merger stage D (Fig. 6), and notably is the nearest broad-absorption line quasar.

While the MIR spectrum of the source does not show evidence of [Ne V] emission lines (Pereira-Santaella et al. 2010; Inami et al. 2013), the presence of a luminous AGN is inferred from the weak 3.3 μm (EW =8 nm, Imanishi et al. 2010) and 6.2 μm (EW =0.01 μm, Stierwalt et al. 2013) PAH features and from the MIR colours ($W1 - W2 \sim 1.1$). In the optical band, the source is classified as a Seyfert 1 (Yuan et al. 2010). Studying several different tracers of AGN emission, Veilleux et al. (2009) found that the AGN contributes to ∼71 per cent of the bolometric output of the system. A lower value (∼34 per cent) was obtained by Nardini et al. (2010) using spectral decomposition. Mrk 231 is also known to have a strong kpc-scale outflow (Rupke & Veilleux 2013; Feruglio et al. 2015), which has been interpreted as proof of quasar-mode feedback (Feruglio et al. 2010).

The broad-band 0.5–30 keV *NuSTAR* and *Chandra* spectrum of the source was studied by Teng et al. (2014), who found that the primary X-ray continuum is flat, and the X-ray source is obscured by Compton-thin material. Teng et al. (2014) found that the source is X-ray weak, with the 2–10 keV to bolometric luminosity ratio being ∼0.03 per cent (compared to a typical value for local Seyferts of ∼5 per cent, e.g. Vasudevan & Fabian 2007). The values of the column density were found to vary between the 2003 *Chandra* ($19.4^{+5.7}_{-4.4} \times 10^{22}$ cm$^{-2}$) and the 2012 *Chandra*/*NuSTAR* ($9.5^{+2.3}_{-1.9} \times 10^{22}$ cm$^{-2}$) observations. Since we are interested in studying the global properties of AGN in mergers, here we used the average of the two values of the column density.

### A16 IRAS F12590+2934 (NGC 4922N and NGC 4922S)

This merger stage C system includes a LIRG (NGC 4922N) and a nucleus significantly weaker in the IR [NGC 4922S, $\log(L_{\rm IR}/L_{\odot}) = 8.87$]. The two nuclei have a projected separation of 10.8 kpc (Fig. 6). Significant [Ne V] 14.32 μm emission is observed from the system (Inami et al. 2013), while only an upper limit was reported for the 24.32 μm line (Pereira-Santaella et al. 2010). The presence of an AGN in the northern nucleus is suggested by the *WISE* colours ($W1 - W2 = 1.26$, $W2 = 9.42$ mag), while the southern nucleus does not present evidence of a dominating AGN component in the MIR ($W1 - W2 = -0.04$). The system is classified as a Seyfert 2 (Yuan et al. 2010), and shows a weak 6.2 μm PAH feature (EW = 0.16 μm; Stierwalt et al. 2013). The depth of the 9.7 μm silicate feature is $\tau_{9.7\mu m} = -0.60$ (Stierwalt et al. 2013), possibly indicating a buried AGN.

The two nuclei are at a distance of 21.2 arcsec, and could be well resolved by *Chandra*. While in the optical, NGC 4922S is significantly brighter than NGC 4922N, the galaxy is detected by *Chandra* only in the 0.3–2 keV band. NGC 4922N is detected both in the 0.3–2 and 2–10 keV band. A source at a position coincident with NGC 4922N is detected by *NuSTAR* at 4.2$\sigma$ and 4.6$\sigma$ in the 3–10 keV band for FPMA and FPMB, respectively. In the 10–24 keV band, the system is detected at 3.3$\sigma$ in both detectors. Considering the position of the *NuSTAR* source, the fact that NGC 4922S is not detected in the 2–10 keV, and the similar flux level of the *NuSTAR* source with NGC 4922N in the overlapping energy band, we conclude that the source detected by *NuSTAR* is NGC 4922N. The X-ray spectrum of NGC 4922N shows a prominent Fe K$\alpha$ line at $6.48^{+0.07}_{-0.07}$ keV. Fitting the combined 2–24 keV *Chandra*/*NuSTAR* spectrum with a power-law plus a Gaussian line, we find that the line has an EW of $3.0^{+1.4}_{-1.3}$ keV and the X-ray continuum is very hard ($\Gamma = 0.2 \pm 0.4$). Using the Torus model together with a scattered component and a thermal plasma (CONST × ZPOWERLAW+ATABLE{TORUS1006.FITS} + ZPHABS × APEC), we find that the X-ray source is CT ($N_{\rm H} \geq 4.27 \times 10^{24}$ cm$^{-2}$), in agreement with the flat X-ray spectrum and the strong Fe K$\alpha$ line. The torus half-opening angle could not be constrained, and was therefore fixed to $\theta_{\rm OA} = 60$ deg in the model. The fraction of scattered radiation is $f_{\rm scatt} \lesssim 0.5$ per cent. The broad-band X-ray spectrum of NGC 4922N is shown in Fig. B2.

### A17 IRAS 13120−5453

This ULIRG in merger stage D shows a single nucleus (Fig. 6). The presence of an AGN is inferred from the *WISE* colours ($W1 - W2 = 0.86$, $W2 = 8.85$ mag) and from the Seyfert 2 optical classification (Véron-Cetty & Véron 2010). The spectral decomposition study of Nardini et al. (2010) found that the AGN does not contribute significantly to the bolometric output of the system (<1.1 per cent).

The system was detected by *Chandra* (Iwasawa et al. 2011b) and more recently by *NuSTAR* (Teng et al. 2015) up to 20 keV. The X-ray spectral analysis of the combined *Chandra* and *NuSTAR* spectrum of the source found that the AGN is CT, with a line-of-sight column density of $N_{\rm H} \sim 3.2 \times 10^{24}$ cm$^{-2}$ (Teng et al. 2015).

### A18 IRAS F13197−1627 (MCG−03 − 34 −064 and MCG−03 − 34 −063)

This system is composed of the LIRG MCG−03 − 34 −064 and the normal galaxy MCG−03 − 34 −063. The two galaxies are located at a projected distance of 37.7 kpc, and are reported as being in merger stage A. The presence of an AGN in MCG−03 − 34 −064 is confirmed by the detection of the 14.32 and 24.32 μm [Ne V] emission lines (Pereira-Santaella et al. 2010; Inami et al. 2013), and by the very weak (EW<0.01$\mu$m) 6.2 μm PAH feature (Stierwalt et al. 2013). The optical spectrum of this source is consistent with that of an H II region (Yuan et al. 2010).

The two galaxies are separated by 106.2 arcsec, and could be clearly resolved by *XMM–Newton*/EPIC. While, MCG−03 − 34 −063 is not detected in the X-rays, MCG−03 − 34 −064 is clearly detected by *XMM–Newton*, and it was associated with the *Swift*/BAT source. The X-ray spectrum of MCG−03 − 34 −064 is dominated by the emission from the AGN (Miniutti et al. 2007). We fitted the combined *XMM–Newton* EPIC and *Swift*/BAT spectra with a model that includes both absorption and reflection from a torus, a scattered component, three thermal plasmas and two Gaussian lines (ATABLE{TORUS1006.FITS} + 3×APEC + 2×ZGAUSS + ZPOWERLAW; Fig. B2). We find that, in agreement with the results of Miniutti et al. (2007), the X-ray source is obscured by Compton-thin material ($N_{\rm H} = 5.42^{+0.07}_{-0.09} \times 10^{23}$ cm$^{-2}$). The half-opening angle of the torus is $\theta_{\rm OA} = 79.1^{+0.1}_{-2.3}$ deg, while only an upper limit is obtained for the fraction of scattered radiation (≤0.2 per cent). The two Gaussian lines have energies of $1.86^{+0.01}_{-0.01}$ and $6.62^{+0.01}_{-0.01}$ keV, with an EW of $40^{+4}_{-30}$ and $197^{+21}_{-40}$ eV, respectively.

### A19 IRAS 13428+5608 (Mrk 273)

The ULIRG Mrk 273 is a late-merger system (stage D, Fig. 7) composed of two nuclei located separated by 0.7 kpc from each other (Scoville et al. 2000). The MIR spectrum of the source shows a 14.32 μm [Ne V] emission line (Inami et al. 2013). The presence of an AGN is confirmed by the *WISE* colour ($W1 - W2 = 1.182$, $W2 = 9.23$ mag), by radio spectral index maps (Vardoulaki et al. 2015) and by the weak 6.2 μm PAH feature (EW =0.12 μm, Stierwalt et al. 2013). The source is classified as a Seyfert 2 in the optical (Veilleux, Kim & Sanders 1999).

Iwasawa et al. (2011a) discussed the analysis of the *Chandra* observations of the two nuclei (separated by 0.9 arcsec), and their analysis indicated that the AGN coincides with the south-western nucleus, while the northern nucleus contains a powerful starburst which dominates the far-infrared emission. However, the extended emission in the 6–7 keV range in direction of the northern nucleus might imply the presence of a second obscured AGN. Mrk 273 was clearly detected by *NuSTAR* in a ∼70 ks observation carried out in late 2013. The broad-band *XMM–Newton*/*NuSTAR* X-ray spectrum of this object was recently studied by Teng et al. (2015), who found that the X-ray source is obscured by material with a column density of $N_{\rm H} = 4.4 \pm 0.1 \times 10^{23}$ cm$^{-2}$.

### A20 IRAS 14378−3651

IRAS 14378−3651 is a ULIRG in merger stage D with a single nucleus (Fig. 7). The 14.32 and 24.32 μm [Ne V] lines are not detected (Pereira-Santaella et al. 2010; Inami et al. 2013). The *WISE* $W1 - W2$ colour is above the threshold for AGN activity ($W1 - W2 = 0.87$, $W2 = 11.44$ mag), while from the EW of the 6.2 μm feature (0.39 μm) Stierwalt et al. (2013) estimate a contribution of the AGN to the MIR flux of ∼20 per cent. The study of Nardini et al. (2010), based on spectral decomposition, finds a significantly lower contribution from the AGN to the bolometric luminosity (<1.3 per cent). In the optical band, IRAS 14378−3651 has been classified as a LINER by Kim & Sanders (1998) and as a Seyfert 2 by Duc, Mirabel & Maza (1997).

The source was detected by *Chandra*, and Iwasawa et al. (2011b) argued that the hard X-ray colour implies the presence of an AGN with a relatively low 2–10 keV luminosity. From the small ratio between the 2–10 keV and the IR luminosity, Iwasawa et al. (2011b) proposed that the AGN is a CT candidate. The source was observed by *NuSTAR* for 24.5 ks, and was weakly detected only in the 3–10 keV band (Teng et al. 2015), thereby providing no additional constraints beyond those obtained by *Chandra*.

### A21 IRAS F14544−4255 (IC 4518A and IC 4518B)

IRAS F14544−4255 is a LIRG which is composed of two galaxies (IC 4518A and IC 4518B) at a projected separation of 12.0 kpc (Fig. 7). The system is classified as an early merger (stage B). Both the 14.32 μm and the 24.32 μm [Ne V] emission lines are observed in the MIR spectrum of IC 4518A, while they are not detected in that of IC 4518B (Pereira-Santaella et al. 2010; Inami et al. 2013). The 6.2 μm PAH feature of IC 4518A is very weak (EW = 0.05 μm), but is significantly stronger in IC 4518B (EW = 0.47 μm). The *WISE* colour confirms the presence of an AGN in IC 4518A ($W1 - W2 = 1.228$, $W2 = 8.80$ mag), and the galaxy is also classified as a Seyfert 2 in the optical (Masetti et al. 2008). From spectral decomposition, Hernán-Caballero et al. (2015) found that the contribution from the AGN in IC 4518A to the MIR flux is ∼79 per cent.

The two galaxies are both detected by *XMM–Newton*/EPIC and are at ∼36 arcsec from each other, so that we used a radius of 5 arcsec (20 arcsec) for the spectral extraction of IC 4518B (IC 4518A). IC 4518A was significantly detected both by EPIC/PN and MOS1 on board *XMM–Newton* and by *NuSTAR*. The EPIC/MOS2 spectrum could not be extracted since the inner chip where the source was located was not available during this observation. The spectrum was fitted with the same model we used for other AGN (ATABLE{TORUS1006.FITS} + APEC + ZPOWERLAW). The model reproduces well the X-ray spectrum, and we find a column density of $N_{\rm H} = (2.4 \pm 0.2) \times 10^{23}$ cm$^{-2}$ in the direction of the X-ray source. The fraction of scattered radiation is $f_{\rm scatt} = 2.1^{+0.4}_{-0.3}$ per cent, and only an upper limit is obtained for the half-opening angle of the torus ($\theta_{\rm tor} \leq 34$ deg). We found that the cross-correlation constant for the EPIC/PN and MOS1 spectra is ∼0.4, which implies that the source was ∼2.5 times dimmer than at the time of the *NuSTAR* observation. IC 4518B is detected only by EPIC/PN. Due to the low signal-to-noise ratio, the spectrum was rebinned to 1 count per bin and we applied Cash statistics. The X-ray spectrum shows a strong Fe K$\alpha$ line at ∼6.4 keV (EW $= 554^{+319}_{-240}$ eV), and a very flat 2–10 keV continuum ($\Gamma = 0.23^{+0.61}_{-0.62}$), both clear indications of the presence of a buried AGN. We applied the same model as for IC 4518A, with the addition of an absorption component for the thermal plasma and the scattered component [ATABLE{TORUS1006.FITS} + ZPHABS×(APEC + ZPOWERLAW)]. Due to the low signal-to-noise ratio the photon index was fixed to $\Gamma = 1.9$ and the half-opening angle of the torus to 60 deg. We found that the source is obscured by material with a column density of $N_{\rm H} = 3.2^{+4.1}_{-1.4} \times 10^{23}$ cm$^{-2}$, and the scattered flux is $6.8^{+6.9}_{-3.6}$ per cent of the primary X-ray emission. The observed flux of IC 4518B is ∼2 per cent of that of IC 4518A in the 3–10 and 10–24 keV bands, so that its contribution to the *NuSTAR* spectrum can be safely ignored. The spectra of IC 4518A and IC 4518B are shown in Fig. B3.

### A22 IRAS F15327+2340 (Arp 220W and Arp 220E)

Arp 220 is the nearest ULIRG, and is in merger stage D with two nuclei (east and west) separated by only 0.4 kpc (Fig. 7). The presence of at least one AGN in this system has been confirmed by several pieces of observational evidence. The western nucleus is classified as a Seyfert 2 by optical spectroscopy (Yuan et al. 2010). The system shows a weak 6.2 μm PAH feature (EW = 0.17 μm, Stierwalt et al. 2013), which could imply an AGN contribution of ∼30 per cent to the MIR flux. Using six multiwavelength tracers, Veilleux et al. (2009) found that the AGN contributes to ∼18.5 per cent of the bolometric flux. A similar value ($17^{+2}_{-2}$ per cent) was obtained by Nardini et al. (2010) through spectral decomposition. Studies carried out using CO have confirmed that the western nucleus hosts a deeply buried AGN, with a total column density of $\sim 10^{25}$ cm$^{-2}$ (Downes & Eckart 2007; Scoville et al. 2015). Consistent with this, Stierwalt et al. (2013) found that this source exhibits a deep 9.7 μm silicate absorption feature ($\tau_{9.7\,\mu{\rm m}} = -2.26$).

The two nuclei are separated by 1 arcsec, and *Chandra* observations have shown that the peak of the 2–7 keV emission is in the western nucleus (Iwasawa et al. 2011b), while no emission is observed in the same band where the eastern nucleus lies. In the X-ray band, Arp 220 has been shown to have a flat X-ray continuum ($\Gamma \sim 1$, Ptak et al. 2003; Iwasawa et al. 2005) and a strong emission line at 6.7 keV (EW ∼ 1.9 keV, Iwasawa et al. 2005). *NuSTAR*-detected X-ray emission from Arp 220 up to 20 keV (Teng et al. 2015), and using a torus model yields only a lower limit on the column density of $N_{\rm H} \geq 5.3 \times 10^{24}$ cm$^{-2}$, consistent with the results obtained by CO studies. Teng et al. (2015) discuss that the X-ray spectrum could also be well reproduced by a combination of thermal plasma models. However, given the strong evidence for an AGN obtained at other wavelengths, we consider here that the hard X-ray emission is produced by the AGN in Arp 220W.

### A23 IRAS 16504+0228 (NGC 6240N and NGC 6240S)

IRAS 16504+0228 is a LIRG in merger stage D with two nuclei (NGC 6240N and NGC 6240s) separated by 0.7 kpc (Fig. 7). The

system shows a 14.32 μm [Ne V] emission line, and in the optical is classified as a LINER (Yuan et al. 2010). The contribution of AGN activity to the bolometric luminosity has been estimated to be ∼26 per cent (Veilleux et al. 2009).

The two nuclei are separated by 1.4 arcsec, and were both detected by *Chandra* observations (Komossa et al. 2003). The presence of an AGN has been confirmed by several studies carried out in the X-ray band (Iwasawa & Comastri 1998; Vignati et al. 1999; Lira et al. 2002b). *Chandra* observations have shown that NGC 6240S is brighter than NGC 6240N, and that both nuclei host CT AGN (Komossa et al. 2003). Combining *Chandra*, *XMM–Newton* and *BeppoSAX* data with recent *NuSTAR* observations, Puccetti et al. (2016) found that both NGC 6240S ($N_{\rm H} = 1.47^{+0.21}_{-0.17} \times 10^{24}$ cm$^{-2}$) and NGC 6240N ($N_{\rm H} = 1.55^{+0.72}_{-0.23} \times 10^{24}$ cm$^{-2}$) host CT AGN.

### A24 IRAS F16577+5900 (NGC 6286 and NGC 6285)

IRAS F16577+5900 is a system composed of a LIRG (NGC 6286) and its companion (NGC 6285), which is significantly less luminous in the IR [$\log(L_{\rm IR}/{\rm L}_{\odot}) = 10.72$]. The two galaxies are in merger stage B and are separated by 35.8 kpc (Fig. 7). None of the tracers of AGN activity show evidence of an accreting SMBH in either nucleus, with the possible exception of faint 14.32 and 24.32 μm [Ne V] emission lines in NGC 6286 (Dudik, Satyapal & Marcu 2009). The detection of these lines, however, was questioned by Inami et al. (2013). Optically, NGC 6286 is classified as a composite (Yuan et al. 2010). Studying the multiwavelength Spectral Energy Distribution (SED) of NGC 6286, Vega et al. (2008) found that an AGN might contribute to ∼5 per cent of the MIR emission of the galaxy.

Given the separation between the two sources (91.1 arcsec), they could be well resolved by *XMM–Newton*/EPIC, *Chandra* and *NuSTAR* observations. A joint analysis of *XMM–Newton*, *Chandra* and *NuSTAR* observations of this system has shown that NGC 6286 contains a buried AGN (Ricci et al. 2016a), with a column density of $N_{\rm H} = 1.1^{+1.1}_{-0.4} \times 10^{24}$ cm$^{-2}$. NGC 6285 was not detected by *NuSTAR*, and the *Chandra* spectrum is well reproduced by a single power-law model (ZPOWERLAW; Fig. B3).

### A25 IRAS F17138−1017

The LIRG IRAS F17138−1017 is a coalesced merger (stage D) showing only one nucleus (Fig. 8). None of the multiwavelength tracers find any evidence of AGN activity in this system, which is optically classified as a composite (Yuan et al. 2010).

The source was detected by *NuSTAR* at the 4.3$\sigma$ and 5$\sigma$ levels in the 3–10 keV band for FPMA and FPMB, respectively, but remains undetected in the 10–24 keV band. Given the non-detection above 10 keV, we modelled only the 3–10 keV region of the *NuSTAR* spectrum. The combined *Chandra* and *NuSTAR* spectra can be well fit with a simple power-law model (ZPOWERLAW) with a photon index of $\Gamma = 1.13^{+0.17}_{-0.16}$. This is harder than the typical X-ray emission observed for star-forming regions. While we cannot exclude the presence of a low-luminosity or heavily obscured AGN in this object, both the multiwavelength tracers and the low 2–10 keV X-ray luminosity [$\log(L_{2-10}/{\rm erg\,s^{-1}}) = 40.99$] are consistent with a star-forming galaxy. The X-ray spectrum of the source is shown in Fig. B3.

### A26 IRAS 20264+2533 (MCG +04−48 −002 and NGC 6921)

IRAS 20264+2533 is an early merger (stage A) composed of two galaxies with a projected separation of 27.1 kpc: NGC 6921 and the LIRG MCG +04−48 −002 (Fig. 8). The presence of an AGN in MCG +04−48 −002 is suggested by the detection of [Ne V] 14.32 μm, although the source is found to be an H II region in the optical (Masetti et al. 2006).

The two galaxies are separated by 91.4 arcsec, and could therefore be resolved by both *XMM–Newton*/EPIC and *NuSTAR* observations. X-ray observations of these two sources were recently discussed by Koss et al. (2016a), who found both sources to host obscured AGN. Both objects show Fe K$\alpha$ lines at 6.4 keV, and this feature is particularly prominent in NGC 6921. We studied the combined *XMM–Newton* and *NuSTAR* spectrum of each source using the same combination of models applied to other AGN (ZPOWERLAW+ATABLE{TORUS1006.FITS} +APEC). For MCG +04−48 −002, we found that the flux of the primary X-ray emission during the *NuSTAR* observation was about one-fourth of that measured by the *XMM–Newton* observation (the cross-calibration constants were 0.27 ± 0.03 and 0.26 ± 0.03 for FPMA and FPMB, respectively). The X-ray source is obscured by material with a column density of $N_{\rm H} = 5.8^{+0.7}_{-0.4} \times 10^{23}$ cm$^{-2}$, while the ratio between scattered radiation and primary X-ray emission is found to be ≤0.3 per cent. We also constrain the half-opening angle of the torus to be $\theta_{\rm OA} = 78^{+1.0}_{-0.4}$ deg. Previous observations of NGC 6921 found that the galaxy hosts a CT AGN (Ricci et al. 2015; Koss et al. 2016a). Our spectral analysis confirms this result. Applying the same model we used for MCG +04−48 −002, we obtained a column density in the direction of the X-ray source of $N_{\rm H} = 1.78^{+0.30}_{-0.53} \times 10^{24}$ cm$^{-2}$. The scattered radiation is ≤0.6 per cent of the primary component, while the half-opening angle of the torus is $\theta_{\rm OA} = 55^{+16}_{-16}$ deg. The broad-band X-ray spectra of these two sources are shown in Fig. B3.

### A27 IRAS F21453−3511 (NGC 7130)

The LIRG IRAS F21453−3511 is in merger stage D with a single nucleus (Fig. 8). The MIR spectrum of the source shows [Ne V] 14.32 and 24.32 μm emission lines (Pereira-Santaella et al. 2010; Inami et al. 2013), clear indications of AGN activity. The galaxy is classified as a Seyfert 2 (Yuan et al. 2010), and from the 6.2 μm PAH feature Stierwalt et al. (2013) suggested that the AGN contributes ∼40 per cent of the MIR flux. From spectral decomposition, Hernán-Caballero et al. (2015) concluded that ∼51 per cent of the MIR luminosity is due to the AGN.

Studying a *Chandra* observation, Levenson et al. (2005) found that the galaxy hosts a CT AGN. This was also confirmed by Gilli et al. (2010) using the X-ray to [Ne V]3426 flux ratio. Our analysis of the combined *Chandra* and *NuSTAR* spectrum confirms the heavy obscuration of this source, which shows a very strong Fe K$\alpha$ line at 6.4 keV (EW = $1.10^{+0.27}_{-0.22}$ keV). Using the torus model plus two different thermal plasmas [ZPOWERLAW+ATABLE{TORUS1006.FITS} + ZPHABS×(APEC+APEC)], we found a column density of $N_{\rm H} = 4.07^{+1.52}_{-0.91} \times 10^{24}$ cm$^{-2}$ and that 0.3 ± 0.2 per cent of the primary X-ray radiation is scattered. Only an upper limit for the half-opening angle of the torus could be obtained by our analysis ($\theta_{\rm OA} \leq$ 37 deg). The broad-band X-ray spectrum of NGC 7130 is presented in Fig. B4.

### A28 IRAS F23007+0836 (NGC 7469 and IC 5283)

IRAS F23007+0836 is a system composed of a pair of galaxies in an early merger (stage A) at a projected distance of 26 kpc (Fig. 8). NGC 7469 is a LIRG, while IC 5283 has a lower IR luminosity ($\log L_{\rm IR} = 10.79\,{\rm L}_{\odot}$). The presence of an AGN in NGC 7469 has been confirmed by several tracers. The MIR spectrum shows

both 14.32 and 24.32 μm [Ne V] emission lines (Pereira-Santaella et al. 2010; Inami et al. 2013), and weak 3.3 μm (EW =32 nm) and 6.2 μm (EW= 0.23 μm) PAH features (Stierwalt et al. 2013; Yamada et al. 2013). The AGN is optically classified as a Seyfert 1 (Yuan et al. 2010), and it has been estimated that it contributes ∼64 per cent of the MIR flux.

The two galaxies are separated by 79.7 arcsec, and could therefore be resolved by *XMM–Newton*/EPIC, *NuSTAR* and *Swift*/XRT observations. Previous X-ray studies of NGC 7469 carried out using *XMM–Newton* (Blustin et al. 2003; Scott et al. 2005) and *Suzaku* (Walton et al. 2013) have shown that the AGN is obscured only by ionized material, in agreement with the optical classification. To constrain the level of obscuration of the source, we studied the combined *XMM–Newton* and *Swift*/BAT spectrum. Data from EPIC/MOS were not used because the inner chips of MOS1 and MOS2 were missing during the observation. We used a model that considers reprocessed X-ray emission from a slab [PEXRAV (Magdziarz & Zdziarski 1995)], a Gaussian line for the Fe K$\alpha$ emission (ZGAUSS), a soft excess in the form of a blackbody (BBODY) and ionized absorption (ZXIPCF). The model we used is ZXIPCF×(BBODY + ZGAUSS + ZXIPCF×PEXRAV). We find that the neutral column density in the direction of the source is extremely low [$\log(N_{\rm H}/\,{\rm cm}^{-2}) \sim 19.8$], and the Fe K$\alpha$ line at 6.40 ± 0.01 keV is relatively weak (EW = $81^{+17}_{-14}$ eV). The two ionized absorbers have column densities of $N_{\rm H}^{\rm W,1} = 1.7^{+6.6}_{-0.6} \times 10^{21}\,{\rm cm}^{-2}$ and $N_{\rm H}^{\rm W,2} = 1.8^{+0.5}_{-0.2} \times 10^{23}\,{\rm cm}^{-2}$, ionization parameters of $\log(\xi^1/{\rm erg\,cm\,s}^{-1}) = 2.36 \pm 0.07$ and $\log(\xi^2/{\rm erg\,cm\,s}^{-1}) \geq -0.20$, and cover a fraction of $f^1 \geq 37$ per cent and $f^2 = 32^{+2}_{-4}$ per cent of the X-ray source. The temperature of the blackbody component is $kT = 0.106 \pm 0.002$ eV, while the reflection parameter is $R = 0.77^{+0.41}_{-0.34}$. The X-ray spectrum of NGC 7469 is shown in Fig. B4.

The EPIC/PN observation of IRAS F23007+0836 was carried out in small-window mode, and therefore IC 5283 fell outside of the limited Field of View (FOV) of this *XMM–Newton* observation. We therefore analysed the *Swift*/XRT image of the field, but found that IC 5283 is not detected either in the 0.3–2 or in the 2–10 keV band.

### A29 IRAS F23254+0830 (NGC 7674 and NGC 7674A)

IRAS F23254+0830 is a galaxy pair in merger stage A, with the two galaxies having a separation of 20.7 kpc (Fig. 8). NGC 7674 is a LIRG, while NGC 7674A has an IR luminosity of $\log(L_{\rm IR}/{\rm L}_\odot) = 10.01$. The presence of an AGN in NGC 7674 is confirmed by several proxies. Both [Ne V] 14.32 and 24.32 μm are significantly detected (Pereira-Santaella et al. 2010; Inami et al. 2013). The *W*1 − *W*2 *WISE* colour is above the threshold (*W*1 − *W*2 = 1.16, *W*2 = 8.11 mag), and the NIR slope shows a red continuum ($\Gamma_{2.5-5\mu{\rm m}} = 1.4$, Imanishi et al. 2010). Both the 3.3 μm (EW =21 nm) and the 6.2 μm (EW = 0.02 μm) PAH features are weak (Imanishi et al. 2010; Stierwalt et al. 2013). Optical spectroscopy studies have classified NGC 7674 as a Seyfert 2 (Yuan et al. 2010).

NGC 7674A, which is located at 34.1 arcsec from NGC 7674, is not detected in the X-ray band by observations carried out with *Swift*/XRT, which would be able to resolve the two sources (Gandhi et al. 2016). A *NuSTAR* observation of NGC 7674, combined with *Suzaku*/XIS and *Swift*/XRT observations, was recently studied by Gandhi et al. (2016). In this work, it was found that, although the Fe K$\alpha$ line is relatively weak (EW =400 eV), the AGN is CT and possibly reflection dominated, with a line-of-sight column density of $N_{\rm H} \gtrsim 3 \times 10^{24}\,{\rm cm}^{-2}$.

### A30 IRAS 23262+0314 (NGC 7679 and NGC 7682)

IRAS 23262+0314 is a system in an early merger (stage A) with the two galaxies (NGC 7679 and NGC 7682) separated by 97.3 kpc (Fig. 8). NGC 7679 is a LIRG which shows a 14.32 μm [Ne V] emission line (Inami et al. 2013) and is optically classified as a Seyfert 2 (Yuan et al. 2010). Spectral decomposition studies have shown that the AGN in this galaxy could contribute to ∼19 per cent of the MIR emission (Hernán-Caballero et al. 2015). NGC 7682 is not a luminous IR source and is optically classified as a Seyfert 2 (Huchra & Burg 1992).

The two galaxies are separated by 269.7 arcsec, and could be well resolved by the *XMM–Newton* observations analysed here. NGC 7679 was found to be unobscured with a luminosity of $3.4 \times 10^{42}\,{\rm erg\,s}^{-1}$ in the analysis of a *BeppoSAX* observation (Risaliti 2002; Dadina 2007). The X-ray luminosity is above the threshold typically used to separate AGN from starbursts in the 2–10 keV band ($10^{42}\,{\rm erg\,s}^{-1}$; Kartaltepe et al. 2010). In a subsequent *XMM–Newton* observation, we found the X-ray source was about 10 times dimmer in the 2–10 keV band ($4 \times 10^{41}\,{\rm erg\,s}^{-1}$), and the spectrum could be well modelled with a power-law component, plus a thermal component, a Gaussian line and neutral absorption [ZPHABS×(APEC+PO+ZGAUSS)]. We confirm that the source is unobscured and find that the Gaussian line has an energy of $E = 6.57^{+0.07}_{-0.09}$ keV and an EW of $450^{+171}_{-200}$ eV. The strong X-ray variability indicates the presence of an AGN. Using the relation of Ranalli et al. (2003), we find that a star formation rate of $\sim 80\,{\rm M}_\odot\,{\rm yr}^{-1}$ is needed to account for the 2–10 keV luminosity of the source at the time of the *XMM–Newton* observation. This is ∼4 times larger than the value obtained from H$\alpha$ ($21.2 \pm 0.2\,{\rm M}_\odot\,{\rm yr}^{-1}$, Davies et al. 2016) and ∼8 times that inferred from the 3.6 and 8 μm images ($11.4 \pm 0.6\,{\rm M}_\odot\,{\rm yr}^{-1}$, Davies et al. 2016). The star formation rate needed to reproduce the X-ray luminosity found by Dadina (2007) would be $\sim 680\,{\rm M}_\odot\,{\rm yr}^{-1}$, ∼30–60 times larger than the value observed. We therefore conclude that most of the X-ray emission observed is most likely due to the AGN. NGC 7682 is a known CT AGN (Singh, Shastri & Risaliti 2011; Ricci et al. 2015). We analysed the *XMM–Newton* of this object using a torus model plus scattered emission and a thermal plasma [ZPOWERLAW+ATABLE{TORUS1006.FITS} +ZPHABS×APEC]. Our analysis confirms that the X-ray source is CT, with a column density of $N_{\rm H} = 2.43^{+0.60}_{-0.44} \times 10^{24}\,{\rm cm}^{-2}$. We find that the half-opening angle of the torus is $\theta_{\rm OA} \geq 68$ deg and ≤0.04 per cent of the primary radiation is scattered. The X-ray spectra of NGC 7679 and NGC 7682 are illustrated in Fig. B4.

## APPENDIX B: X-RAY SPECTRA

The X-ray spectra and the best-fitting models are illustrated in Figs B1–B4. For visualization purposes, spectra are typically rebinned to have at least a significance of 3$\sigma$ per bin.

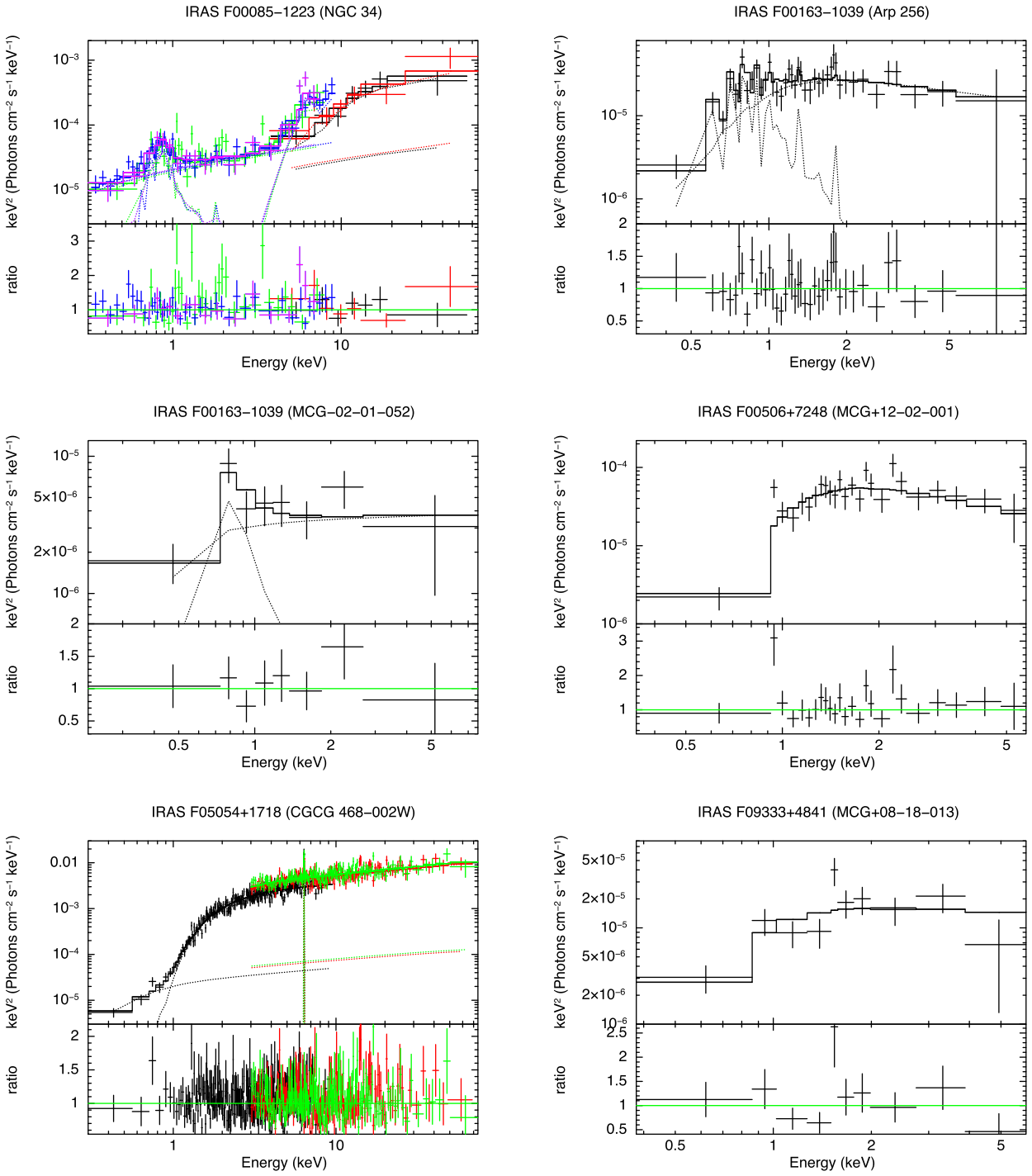


**Figure B1.** X-ray spectra of NGC 34 [*NuSTAR*, *Chandra* and *XMM–Newton*; Section A1, $N_{\rm H} = (5.3 \pm 1.1) \times 10^{23}$ cm$^{-2}$], Arp 256 (*Chandra*; Section A2), MCG−02 − 01 −052 (*Chandra*; Section A2), MCG+12−02 −001 (*Chandra*; Section A3), CGCG 468−002W [*NuSTAR* and *Swift*/XRT; Section A5, $N_{\rm H} = (1.50 \pm 0.09) \times 10^{22}$ cm$^{-2}$] and MCG+08−18 −013 (*Chandra*; Section A9). The bottom panels show the ratio between the data and the models.

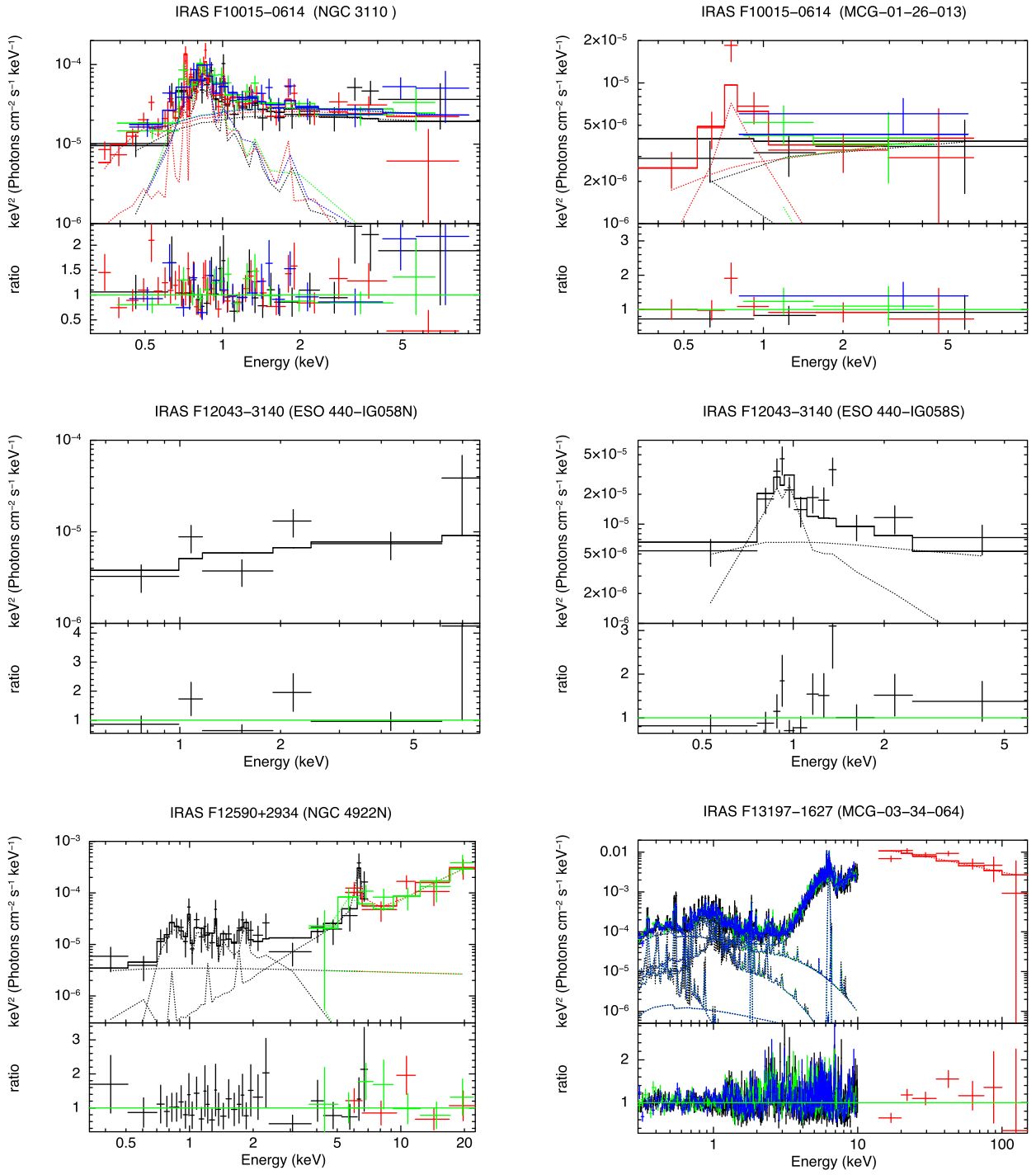


**Figure B2.** X-ray spectra of NGC 3110 (*XMM–Newton* and *Chandra*; Section A10), MCG−01 − 26 −013 (*XMM–Newton* and *Chandra*, Section A10), ESO 440−IG058N (*Chandra*; Section A14), ESO 440−IG058S (*Chandra*; Section A14), NGC 4922N (*NuSTAR* and *Chandra*; Section A16, $N_{\rm H} \geq 4.27 \times 10^{24}$ cm$^{-2}$), and MCG−03 − 34 −064 [*XMM–Newton* EPIC and *Swift*/BAT; Section A18, $N_{\rm H} = (54.2^{+0.7}_{-0.9}) \times 10^{22}$ cm$^{-2}$].

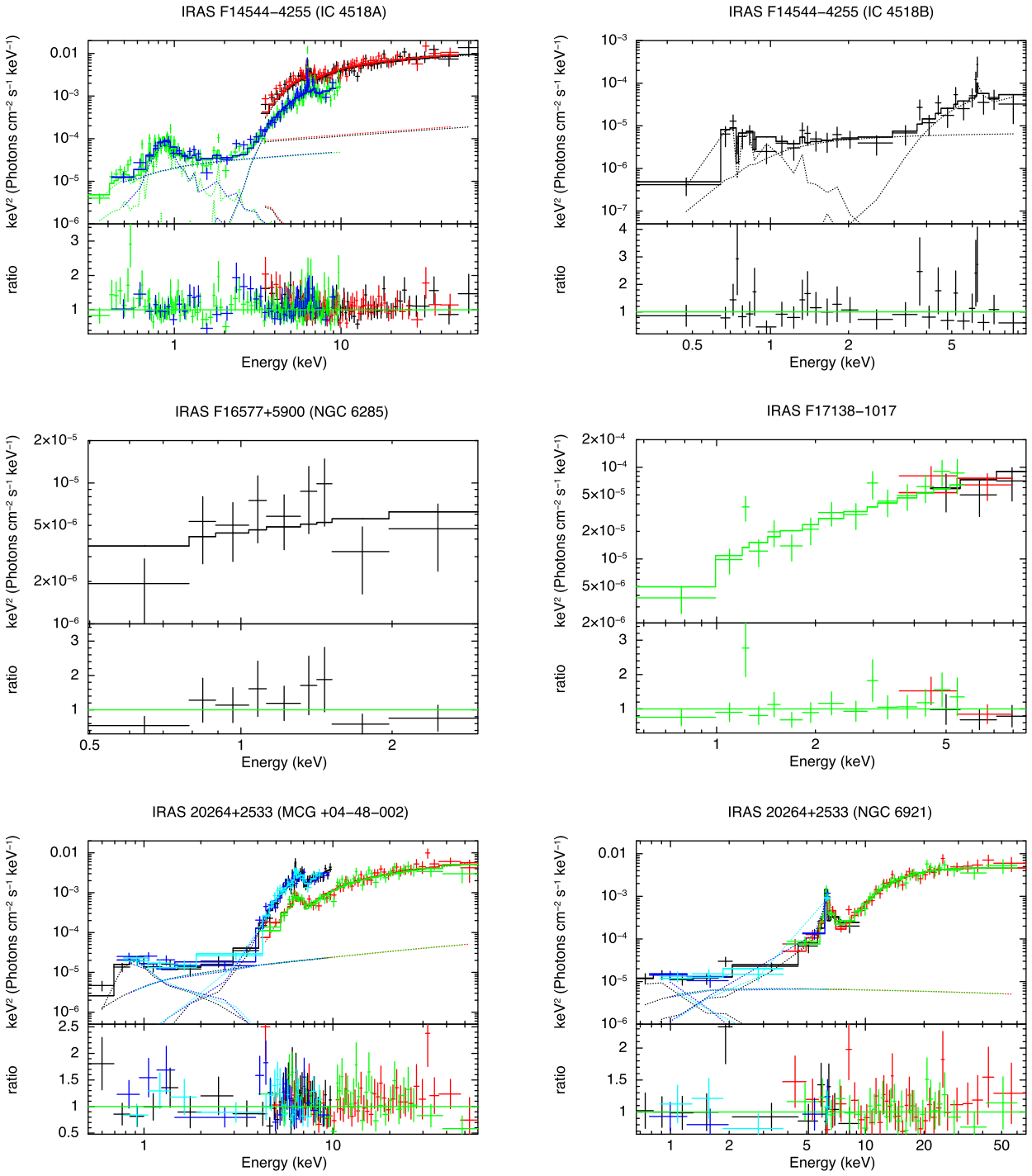


**Figure B3.** X-ray spectra of IC 4518A [*NuSTAR* and *XMM–Newton*; Section A21, $N_{\rm H} = (2.4 \pm 0.2) \times 10^{23}$ cm$^{-2}$], IC 4518B [*XMM–Newton*; Section A21, $N_{\rm H} = (3.2^{+4.1}_{-1.4}) \times 10^{23}$ cm$^{-2}$], NGC 6285 (*Chandra*, Section A24), IRAS F17138−1017 (*NuSTAR* and *Chandra*; Section A25), MCG +04−48 −002 [*NuSTAR* and *XMM–Newton*, Section A26, $N_{\rm H} = (5.8^{+0.7}_{-0.4}) \times 10^{23}$ cm$^{-2}$], and NGC 6921 (*NuSTAR* and *XMM–Newton*, Section A26, $N_{\rm H} = (1.78^{+0.30}_{-0.53}) \times 10^{24}$ cm$^{-2}$).

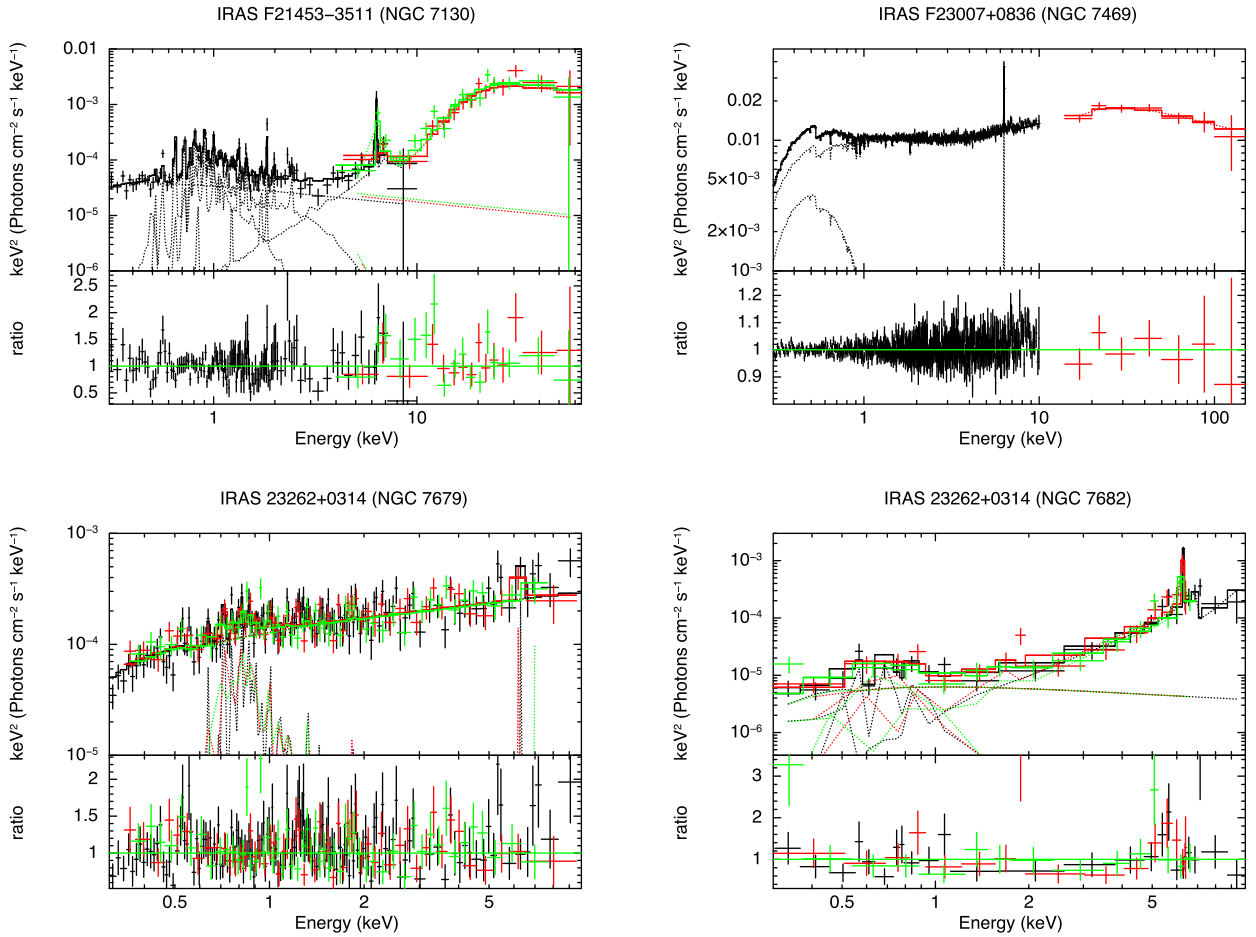


**Figure B4.** X-ray spectra of NGC 7130 [*NuSTAR* and *Chandra*; Section A27, $N_{\rm H} = (4.07^{+1.52}_{-0.91}) \times 10^{24}\,{\rm cm}^{-2}$], NGC 7469 [*XMM–Newton* and *Swift*/BAT; Section A28, $N_{\rm H} = (6 \pm 2) \times 10^{19}\,{\rm cm}^{-2}$], NGC 7679 [*XMM–Newton*; Section A30, $N_{\rm H} \leq 2 \times 10^{20}\,{\rm cm}^{-2}$], and NGC 7682 [*XMM–Newton*; Section A30, $N_{\rm H} = (2.43^{+0.60}_{-0.44}) \times 10^{24}\,{\rm cm}^{-2}$].

This paper has been typeset from a TEX/LATEX file prepared by the author.